Available online at www.sciencedirect.com
ScienceDirect
Journal of Sound and Vibration 314 (2008) 113–146
JOURNAL OF SOUND AND VIBRATION
www.elsevier.com/locate/jsvi

Rayleigh Lecture 2007: Flow-surface interaction noise ☆

M.S. Howe

College of Engineering, Boston University, 110 Cummington Street, Boston, MA 02215, USA

Received 24 October 2007; received in revised form 25 December 2007; accepted 27 December 2007
Handling Editor: P. Joseph
Available online 13 February 2008

Abstract

A review is given of the theory of vortex sound with emphasis on sound production by vortex–surface interactions involving rigid and deformable, compact and noncompact moving bodies. The analysis is facilitated by use of the 'compact' approximation to the acoustic Green's function in cases where the solid surface is either acoustically compact or, for noncompact bodies, where the surface supports locally compact regions of 'noisy' flow identified by the presence of singularities in the 'Kirchhoff vector' of Green's function. The noncompact problem of the compression wave generated by a high-speed train entering a tunnel is discussed as an example of how accurate predictions of sound generation by identified distributions of vorticity can frequently be made by analytical means when the more conventional numerical approach becomes intractable.

1. Introduction

1.1. Equations of aerodynamic sound

Motion within an unbounded homogeneous fluid, which is at rest at infinity, is possible only in the presence of vorticity. If the fluid is compressible a small fraction of the kinetic energy of the vortex field will radiate away as sound. This is the problem treated by Lighthill [1] in his original theory of aerodynamic sound. It was argued, that although turbulence is typically produced by flow over a solid boundary or by the instability of a free shear layer, the influence of boundaries on the production of sound, as opposed to the production of vorticity, can often be ignored. The theoretical problem was accordingly reduced to the study of the free-field mechanism involved in the conversion of rotational kinetic energy into acoustic waves that propagate as longitudinal vibrations of fluid particles. Lighthill unambiguously identified the source of sound at low Mach number to be fluctuations in the turbulence Reynolds stress. Shortly after, Powell [2] proposed for low Mach number flows an explicit vortex representation of the acoustic source.

Most flows of technological interest are of high Reynolds number and turbulent. Lighthill represented the acoustic sources in a turbulent fluid of density $\rho(\mathbf{x}, t)$ and velocity $v_i(\mathbf{x}, t)$ by a distribution of 'quadrupoles' whose strength per unit volume is dominated by the Reynolds stress $\rho v_i v_j$. He did this by establishing an exact

☆ Delivered at the Autumn Conference of the Institute of Acoustics, Oxford, 17–18 October 2007.

E-mail address: mshowe@bu.edu

0022-460X/$ - see front matter © 2008 Elsevier Ltd. All rights reserved.
doi:10.1016/j.jsv.2007.12.035

analogy between the production of sound by turbulence in a fluid whose mean pressure, density and sound speed are, respectively p_o, ρ_o and c_o at large distances from the source flow, and that produced in an ideal, stationary acoustic medium (of mean pressure, density and sound speed equal to p_o, ρ_o and c_o, respectively) forced by the stress distribution

$$T_{ij} = \rho v_i v_j + ((p - p_o) - c_o^2(\rho - \rho_o))\delta_{ij} - \sigma_{ij}, \tag{1}$$

where p is the pressure and σ_{ij} is the viscous stress. T_{ij} is the *Lighthill stress tensor*, which determines the quadrupole source strength in Lighthill's equation

$$\left(\frac{1}{c_o^2}\frac{\partial^2}{\partial t^2} - \nabla^2\right)[c_o^2(\rho - \rho_o)] = \frac{\partial^2 T_{ij}}{\partial x_i \partial x_j}. \tag{2}$$

Fluctuations in $c_o^2(\rho - \rho_o)$ are generated by the stress distribution $T_{ij}(\mathbf{x}, t)$ and propagate away as sound waves from the turbulent source flow. In the distant field the background is quiescent and unsteady motions consist entirely of small-amplitude pressure perturbations $p(\mathbf{x}, t) - p_o \equiv c_o^2(\rho(\mathbf{x}, t) - \rho_o)$.

Lighthill's equation is an *exact* rearrangement and combination of the momentum and continuity equations. It represents an effective means of calculating the sound produced by turbulence only when T_{ij} is known. The Lighthill tensor T_{ij} actually accounts not only for the production of sound but also for its nonlinear self-modulation, for its convection, scattering and refraction by the turbulence and by sound speed variations, and for its attenuation by thermal and viscous diffusion. In many applications nonlinearity is sufficiently weak to be neglected within the source region, although it may cumulatively affect propagation to a distant observer. Convection and refraction are important for turbulence contained in an extensive mean shear layer or adjacent to a large, quiescent region whose mean thermodynamic properties differ from those in the radiation zone, and correspond to contributions to T_{ij} from *linear* perturbations of the mean background flow. Safe predictions can be made using Lighthill's equation, provided all of these effects are small or are sufficiently well understood to be explicitly included in T_{ij}, either analytically [3–5] or from data derived from the numerical modelling of *compressible* motions in the source region. When this is not possible predictions of Lighthill's equation are strictly valid only when the characteristic Mach number M satisfies $M^2 \ll 1$.

Lighthill's equation can be recast so that vorticity is explicitly identified as the ultimate source of sound by adopting the *total enthalpy* B as the acoustic variable instead of Lighthill's $c_o^2(\rho - \rho_o)$ [6,7]. The sources are then confined to regions where the vorticity $\boldsymbol{\omega} \neq \mathbf{0}$ and where $\nabla s \neq \mathbf{0}$, where s is the entropy. In the important case where the source flow is effectively *homentropic* (e.g. in a homogeneous fluid with no combustion), the modified Lighthill equation reduces to

$$\left(\frac{\mathrm{D}}{\mathrm{D}t}\left(\frac{1}{c^2}\frac{\mathrm{D}}{\mathrm{D}t}\right) - \frac{1}{\rho}\nabla\cdot(\rho\nabla)\right)B = \frac{1}{\rho}\,\mathrm{div}(\rho\boldsymbol{\omega}\wedge\mathbf{v}), \tag{3}$$

where $\boldsymbol{\omega}\wedge\mathbf{v}$ is the *Lamb* vector.

For this type of motion $\rho \equiv \rho(p)$ and

$$B = \int \frac{\mathrm{d}p}{\rho} + \frac{1}{2}v^2. \tag{4}$$

Furthermore, from the Bernoulli equation it follows that in the absence of vorticity and moving boundaries B is equal to a constant throughout the fluid that may be assumed to vanish.

Outside the source flow, the unsteady motion is entirely irrotational. It can be represented by a velocity potential $\varphi(\mathbf{x}, t)$, in terms of which $B \equiv -\partial\varphi/\partial t$ determines the amplitude of the propagating sound waves. B is related to the acoustic pressure in the far field by

$$\frac{1}{\rho}\frac{\partial p}{\partial t} = \frac{\mathrm{D}B}{\mathrm{D}t}. \tag{5}$$

When there is no mean flow at infinity $p - p_o = \rho_o B$.

The wave-operator on the left of the vortex sound equation (3) involves terms that account for nonlinear propagation of sound, because the local values of the density ρ, sound speed c and the flow velocity $\mathbf{v}$ are strictly dependent on the acoustic disturbance. Similarly, in a turbulent source flow whose extent exceeds

many characteristic acoustic wavelengths, or where a mean shear layer supplies a large *linear* contribution to the fluctuating part of $\boldsymbol{\omega} \wedge \mathbf{v}$, the vortex source causes scattering and refraction of the sound, and this must be regarded as an implicit component of the vortex source of Eq. (3). When such effects are ignored, the restrictions underlying the use of Eq. (3) are essentially the same as for Lighthill's original form (2).

When M is small, local mean values of ρ and c differ from their uniform respective values ρ_o and c_o by terms of relative order $M^2 \ll 1$. The vortex sound equation (3) is then simplified by putting $c = c_o$ and $\rho = \rho_o$, and by explicitly neglecting nonlinear effects of propagation and the scattering of sound by the vorticity. The production of sound is then governed by

$$\left(\frac{1}{c_o^2}\frac{\partial^2}{\partial t^2} - \nabla^2\right) B = \mathrm{div}(\boldsymbol{\omega} \wedge \mathbf{v}). \tag{6}$$

1.2. Free-field turbulence

The solution with the outgoing wave behaviour of Eq. (2) for Lighthill's problem in which the turbulence resides in an unbounded fluid is the 'retarded potential' integral

$$c_o^2(\rho - \rho_o)(\mathbf{x}, t) = \frac{1}{4\pi}\frac{\partial^2}{\partial x_i \partial x_j}\int_{-\infty}^{\infty} \frac{T_{ij}(\mathbf{y}, t - |\mathbf{x} - \mathbf{y}|/c_o)}{|\mathbf{x} - \mathbf{y}|}\, \mathrm{d}^3\mathbf{y}. \tag{7}$$

Take the coordinate origin within the source flow. In the acoustic region (where $|\mathbf{x}| \gg |\mathbf{y}|$ for all relevant values of $\mathbf{y}$) we can put $p - p_o = c_o^2(\rho - \rho_o)$ and $|\mathbf{x} - \mathbf{y}| \approx |\mathbf{x}| - \mathbf{x}\cdot\mathbf{y}/|\mathbf{x}|$. Therefore, suppressing the irrelevant constant pressure p_o, the acoustic pressure becomes

$$p(\mathbf{x}, t) \approx \frac{x_i x_j}{4\pi c_o^2 |\mathbf{x}|^3}\frac{\partial^2}{\partial t^2}\int T_{ij}\left(\mathbf{y}, t - \frac{|\mathbf{x}|}{c_o} + \frac{\mathbf{x}\cdot\mathbf{y}}{c_o|\mathbf{x}|}\right) \mathrm{d}^3\mathbf{y}, \quad |\mathbf{x}| \to \infty. \tag{8}$$

The sound radiated by uncorrelated 'eddies' in the source flow may be calculated separately for each eddy; the acoustic power for the whole flow is then obtained by simple addition of the separate sound powers. If the source region has volume V_o and a typical eddy has diameter $\sim \ell$ there are $\sim V_o/\ell^3$ statistically independent eddies producing sound of frequency $f \sim v/\ell$ and wavelength $c_o/f \sim \ell/M \gg \ell$, in low Mach number flow where $M \sim v/c_o \ll 1$. Each eddy is therefore *acoustically compact*.

Suppose the integral in Eq. (8) is restricted to the single eddy, and take the origin at O as indicated in Fig. 1. The travel time $|\mathbf{x} - \mathbf{y}|/c_o$ of sound produced by the source element at $\mathbf{y}$ within the eddy differs from the nominal mean travel time $|\mathbf{x}|/c_o$ from O by $\mathbf{x}\cdot\mathbf{y}/c_o|\mathbf{x}|$, and the corresponding acoustic phase difference $\sim f \times (\mathbf{x}\cdot\mathbf{y}/c_o|\mathbf{x}|) \sim M \ll 1$. Thus all parts of the eddy radiate with effectively the same phase, and the retarded time variations $\mathbf{x}\cdot\mathbf{y}/c_o|\mathbf{x}|$ across the eddy can be neglected in the integrand. Hence there is no destructive interference between different contributions to the integral over the eddy and, because $T_{ij} \sim \rho_o v^2$ and $\partial/\partial t \sim f$, the order of magnitude of the acoustic pressure for one eddy is

$$p \sim \frac{\ell}{|\mathbf{x}|}\frac{\rho_o v^4}{c_o^2} = \frac{\ell}{|\mathbf{x}|}\rho_o v^2 M^2. \tag{9}$$

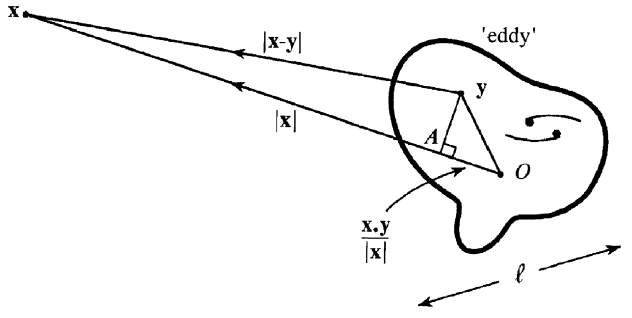

Fig. 1. Radiation from a source at $\mathbf{y}$ to an observer at $\mathbf{x}$ in the acoustic far field.

The acoustic power radiated by the eddy is just the mean acoustic intensity $p^2/\rho_o c_o$ multiplied by the surface area $4\pi|\mathbf{x}|^2$ of a large sphere centred on the eddy $\sim\rho_o v^8\ell^2/c_o^5=\rho_o v^3M^5\ell^2$ — Lighthill's 'eighth power' law [1,8–10]. The total power radiated by the V_o/ℓ^3 eddies in the source flow is therefore $\Pi\sim(\rho_o v^3/\ell)M^5V_o$. But the mechanical power required to maintain the kinetic energy of a statistically steady turbulent source is $\Pi_o\sim(\rho_o v^3/\ell)V_o$ [11], so that the *efficiency* with which turbulence kinetic energy is converted into sound is $\Pi/\Pi_o\sim M^5$. This is smaller than 0.01 for $M<0.4$, confirming Lighthill's hypothesis that sound is an infinitesimal by-product of the turbulent activity.

1.3. Influence of a solid boundary

Let us repeat the steps leading to Lighthill's order of magnitude estimate (9) for the acoustic pressure by starting from the solution of Eq. (6) for the sound generated by a single eddy of diameter ℓ, which we first write in the form

$$p(\mathbf{x},t)=\frac{\rho_o}{4\pi}\int\frac{\partial(\boldsymbol{\omega}\wedge\mathbf{v})_j}{\partial y_j}\left(\mathbf{y},t-\frac{|\mathbf{x}-\mathbf{y}|}{c_o}\right)\frac{\mathrm{d}^3\mathbf{y}}{|\mathbf{x}-\mathbf{y}|}$$
$$\approx\frac{\rho_o}{4\pi|\mathbf{x}|}\int\frac{\partial(\boldsymbol{\omega}\wedge\mathbf{v})_j}{\partial y_j}\left(\mathbf{y},t-\frac{|\mathbf{x}|}{c_o}+\frac{x_iy_i}{c_o|\mathbf{x}|}\right)\mathrm{d}^3\mathbf{y},\quad|\mathbf{x}|\to\infty,\tag{10}$$

where the differential operator $\partial/\partial y_j$ is applied only to the dependence of $(\boldsymbol{\omega}\wedge\mathbf{v})_j(\mathbf{y},\tau)$ on its first argument.

Because the $\boldsymbol{\omega}\equiv 0$ outside the source region, we find by expanding the integrand in powers of the retarded time variation $x_iy_i/c_o|\mathbf{x}|\sim O(\ell/c_o)$ and integrating by parts

$$p(\mathbf{x},t)\approx-\frac{\rho_o x_i}{4\pi c_o|\mathbf{x}|^2}\frac{\partial}{\partial t}\int(\boldsymbol{\omega}\wedge\mathbf{v}\cdot\nabla y_i)\left(\mathbf{y},t-\frac{|\mathbf{x}|}{c_o}\right)\mathrm{d}^3\mathbf{y}$$
$$-\frac{\rho_o x_ix_j}{4\pi c_o^2|\mathbf{x}|^3}\frac{\partial^2}{\partial t^2}\int y_i(\boldsymbol{\omega}\wedge\mathbf{v})_j\left(\mathbf{y},t-\frac{|\mathbf{x}|}{c_o}\right)\mathrm{d}^3\mathbf{y},\quad|\mathbf{x}|\to\infty.\tag{11}$$

The first term on the right-hand side represents dipole radiation and is identically zero when the source flow is regarded as incompressible. This follows from the identity $\boldsymbol{\omega}\wedge\mathbf{v}=(\partial/\partial x_j)(v_j\mathbf{v})-\nabla(\frac{1}{2}v^2)$ for incompressible flow and the condition that the hydrodynamic field vanishes at infinity. The remaining term gives the usual quadrupole sound whose order of magnitude is readily seen to be given by Eq. (9).

These conclusions are altered when the turbulence is adjacent to a solid boundary. Consider first the sound produced by an eddy near an acoustically compact rigid body. The representation (10) becomes [6]

$$p(\mathbf{x},t)=\frac{\rho_o}{4\pi}\int\frac{\partial(\boldsymbol{\omega}\wedge\mathbf{v})_j}{\partial y_j}\left(\mathbf{y},t-\frac{|\mathbf{X}-\mathbf{Y}|}{c_o}\right)\frac{\mathrm{d}^3\mathbf{y}}{|\mathbf{X}-\mathbf{Y}|},$$
$$\text{where}\quad\left.\begin{array}{l}\mathbf{X}=\mathbf{x}-\boldsymbol{\varphi}^*(\mathbf{x})\\ \mathbf{Y}=\mathbf{y}-\boldsymbol{\varphi}^*(\mathbf{y})\end{array}\right\}\ \text{Kirchhoff vectors for the body.}\tag{12}$$

The vector components $X_j(\mathbf{x})$ and $Y_j(\mathbf{y})$ may be interpreted as the velocity potentials of incompressible flow past the body having unit speed in the j-direction at large distances from the body; φ_j^* corresponds to the velocity potential of flow produced by rigid body motion of the body at unit speed in the j-direction, and decreases like $1/(\text{distance})^2$ at large distances from the body.

The first nontrivial term in the expansion of the integrand in Eq. (12) in powers of the retarded time variation is the dipole approximation

$$p(\mathbf{x},t)\approx\frac{\rho_o}{4\pi|\mathbf{x}|}\int\frac{\partial(\boldsymbol{\omega}\wedge\mathbf{v})_j}{\partial y_j}\left(\mathbf{y},t-\frac{|\mathbf{x}|}{c_o}+\frac{x_iY_i}{c_o|\mathbf{x}|}\right)\mathrm{d}^3\mathbf{y}$$
$$\approx-\frac{\rho_o x_i}{4\pi c_o|\mathbf{x}|^2}\frac{\partial}{\partial t}\int(\boldsymbol{\omega}\wedge\mathbf{v}\cdot\nabla Y_i)\left(\mathbf{y},t-\frac{|\mathbf{x}|}{c_o}\right)\mathrm{d}^3\mathbf{y},\quad|\mathbf{x}|\to\infty.\tag{13}$$

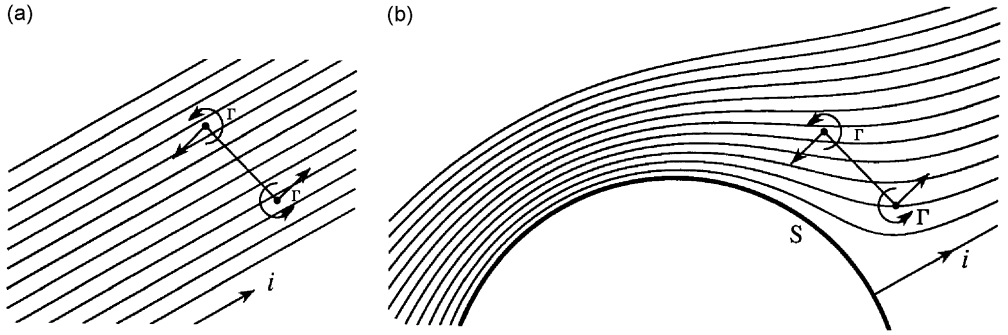

Fig. 2. The dipole strength of a spinning vortex pair is (a) zero in the uniformly spaced streamlines of the 'free space' velocity potential y_i and (b) nonzero when spinning in the nonuniform streamlines of the potential $Y_i = y_i - \varphi_i^*(\mathbf{y})$ defining flow past a curvilinear solid boundary S.

The order of magnitude of the radiation from an eddy of dimension ℓ comparable in size to the solid body is now easily estimated to be $p \sim \rho_o v^2 M(\ell/|\mathbf{x}|)$ [12], which at low Mach numbers exceeds the quadrupole sound produced by a free-field eddy by a factor $\sim O(1/M) \gg 1$. The integral in Eq. (13) is proportional to the i component of the unsteady force exerted on the fluid as a result of the net normal pressure distribution on the body produced by its interaction with the turbulent eddy [6,7]; this force was identified by Curle [12] as determining the amplitude of the dipole radiation.

Fig. 2 gives a graphic illustration of how the shape of the surface S of the solid controls the amplitude of the dipole sound. Here it is supposed that the eddy assumes the form of a 'hydrodynamic test particle' for which the distribution of $\boldsymbol{\omega}$ is locally like a 'spinning' vortex pair [2], where for the two vortices $\boldsymbol{\omega}$ takes the same value, each with total circulation Γ, but their convection velocities $\mathbf{v} = \pm\mathbf{V}$, say, are equal and opposite. For the free-field case, ∇y_i $(= \mathbf{i})$ in the first integral of Eq. (11) defines the uniform streamlines of a hypothetical flow at unit speed in the i-direction. In the integrand $\boldsymbol{\omega} \wedge \mathbf{v} \cdot \nabla y_i \equiv \boldsymbol{\omega} \cdot \mathbf{v} \wedge \nabla y_i$, where for each vortex $\mathbf{v} \wedge \nabla y_i = \pm\mathbf{V} \wedge \nabla y_i$ determines in magnitude and direction the rate at which the vortex cuts across the streamlines of this flow. The aggregate rate evidently vanishes for uniform flow, because ∇y_i is the same for each vortex (Fig. 2a). However, when the vortex pair is near the solid boundary S potential flow streamlines must curve around the body along the direction of the vector field ∇Y_i, which typically assumes different values for each vortex so that cancellation does not occur. The differences for the two vortices become large when S is highly curved (near a sharp edge, say) so that ∇Y_i must then be a rapidly varying function of position assuming very different values for the two vortices [9,13,14].

2. Representation of sound in the presence of a moving body

2.1. Green's function

Sources of sound of dipole type are particularly important in noise control engineering involving *moving* boundaries [6,15,16]. The free-field solutions (7) and (10) or the particular solution (13) for a compact, stationary rigid boundary must then be augmented by additional contributions from sources distributed on the moving boundary. Computationally intensive prediction schemes for aeronautical applications involving high-speed fan and rotor blades are frequently based on the Ffowcs Williams and Hawkings representation of the surface terms for Lighthill's equation (2) [4,17,18]. Surface motions at lower Mach numbers ($M \sim 0.4$ or less) are often more efficiently treated by means of the vortex sound equation (3) [19,20], and this approach is discussed in the remainder of this paper.

Predictions in such cases usually depend on the introduction of an acoustic Green's function $G(\mathbf{x}, \mathbf{y}, t, \tau)$. This satisfies Eq. (3) with the right side replaced by a point source and the wave-operator expressed in a

self-adjoint form (by multiplication by ρ [6,21])

$$\left(\frac{\rho}{\rho_o}\frac{\mathrm{D}}{\mathrm{D}t}\left(\frac{1}{c^2}\frac{\mathrm{D}}{\mathrm{D}t}\right)-\frac{1}{\rho_o}\nabla\cdot(\rho\nabla)\right)G=\delta(\mathbf{x}-\mathbf{y})\delta(t-\tau),\quad G=0\ \text{ for } t<\tau, \tag{14}$$

where the factor $1/\rho_o$ is inserted for convenience.

2.2. General representation of sound

To fix ideas, consider the problem of solving equation (3) in the infinite region V bounded internally by a material control surface S_+ defined by $f(\mathbf{x},t)=0$ (so that $\mathrm{D}f/\mathrm{D}t\equiv 0$) such that $f(\mathbf{x},t)>0$ in the region V outside S_+ (Fig. 3). Assume that any fixed or moving solid boundaries S lie within S_+. Multiply Eq. (3) by $\rho H\equiv\rho H(f)$, where H denotes the Heaviside step function, and form the inhomogeneous equation for the new variable $H\rho_o B$:

$$\left(\frac{\rho}{\rho_o}\frac{\mathrm{D}}{\mathrm{D}t}\left(\frac{1}{c^2}\frac{\mathrm{D}}{\mathrm{D}t}\right)-\frac{1}{\rho_o}\nabla\cdot(\rho\nabla)\right)(H\rho_o B)=\nabla\cdot(H\rho\,\boldsymbol{\omega}\wedge\mathbf{v})+\rho\nabla H\cdot\frac{\partial\mathbf{v}}{\partial t}-\nabla\cdot(\rho B\nabla H)+\eta\nabla\cdot(\nabla H\wedge\boldsymbol{\omega}), \tag{15}$$

where η is the shear coefficient of viscosity and the momentum equation has been used in Crocco's form [6]

$$\frac{\partial\mathbf{v}}{\partial t}+\nabla B=-\boldsymbol{\omega}\wedge\mathbf{v}-\frac{\eta}{\rho}\,\mathrm{curl}\,\boldsymbol{\omega}. \tag{16}$$

Viscosity can usually be ignored in 'noisy' high Reynolds number flows. For this reason the contribution to Crocco's equation (16) from the bulk viscosity has been discarded, because its effect is small everywhere. However, the shear viscosity η is responsible for possibly significant frictional forces on S and is therefore retained, but in doing so it is also assumed that $\eta=$ constant at low Mach numbers.

The first source term on the right of Eq. (15) is distributed in V outside the control surface S_+ (as in Fig. 3). The remaining sources all involve $\nabla H\equiv\nabla f\,\delta(f)$ and are equivalent to *dipole* and *monopole* sources distributed on S_+. The sources determine $H\rho_o B$ *everywhere*, as outgoing acoustic waves at large distances from S_+ and also inside the region bounded by S_+ where $H(f)=0$.

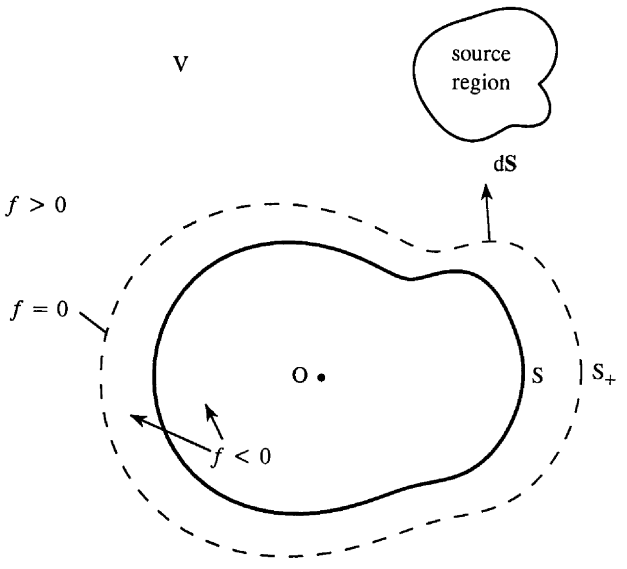

Fig. 3. The material control surface S_+ defined by $f(\mathbf{x},t)=0$ encloses the moving boundary S.

The solution of Eq. (15) can be expressed in terms of *any* causal Green's function $G(\mathbf{x},\mathbf{y},t,\tau)$ that satisfies Eq. (14) for $\mathbf{x}$ and $\mathbf{y}$ within the fluid (outside S in Fig. 3). Then, within the fluid

$$(H\rho_o B)(\mathbf{x},t)=\iint_{-\infty}^{\infty} G(\mathbf{x},\mathbf{y},t,\tau)\Big(\nabla\cdot(H\rho\,\boldsymbol{\omega}\wedge\mathbf{v})-\nabla\cdot(\rho B\nabla H) +\rho\nabla H\cdot\frac{\partial\mathbf{v}}{\partial\tau}+\eta\nabla\cdot(\nabla H\wedge\boldsymbol{\omega})\Big)(\mathbf{y},\tau)\,\mathrm{d}^3\mathbf{y}\,\mathrm{d}\tau, \tag{17}$$

where the integrations can be formally taken over all space and over all values of the retarded time τ. This result is simplified by integrating by parts and by making use of the formula $\int_{-\infty}^{\infty}(\cdot)\nabla H\,\mathrm{d}^3\mathbf{y}=\oint_{S_+}(\cdot)\,\mathrm{d}\mathbf{S}$, where $\mathrm{d}\mathbf{S}$ is the surface element on S_+ directed into the outer region V. The surface S_+ is then allowed to shrink down onto the retarded position of S, thereby yielding for positions $\mathbf{x}$ within the fluid a generalised Kirchhoff integral representation of sound [6,17,22,23]

$$\rho_o B(\mathbf{x},t)=-\iint_V(\rho\,\boldsymbol{\omega}\wedge\mathbf{v})(\mathbf{y},\tau)\cdot\frac{\partial G}{\partial\mathbf{y}}(\mathbf{x},\mathbf{y},t,\tau)\,\mathrm{d}^3\mathbf{y}\,\mathrm{d}\tau+\int\oint_S(\rho B)(\mathbf{y},\tau)\,\frac{\partial G}{\partial\mathbf{y}}(\mathbf{x},\mathbf{y},t,\tau)\cdot\,\mathrm{d}\mathbf{S}\,\mathrm{d}\tau +\int\oint_S G(\mathbf{x},\mathbf{y},t,\tau)\Big(\rho\frac{\partial\mathbf{v}}{\partial\tau}\Big)(\mathbf{y},\tau)\cdot\,\mathrm{d}\mathbf{S}\,\mathrm{d}\tau+\eta\int\oint_S\boldsymbol{\omega}(\mathbf{y},\tau)\wedge\frac{\partial G}{\partial\mathbf{y}}(\mathbf{x},\mathbf{y},t,\tau)\cdot\mathrm{d}\mathbf{S}\,\mathrm{d}\tau. \tag{18}$$

The surface integral involving ρB on the right-hand side is eliminated by requiring the normal derivatives $\partial G/\partial y_n$, $\partial G/\partial x_n$ to vanish, respectively, for $\mathbf{y}$ and $\mathbf{x}$ on S. The remaining terms can then be arranged in the form

$$\rho_o B(\mathbf{x},t)=\int\oint_S G(\mathbf{x},\mathbf{y},t,\tau)\Big(\rho\frac{\partial\mathbf{v}}{\partial\tau}\Big)(\mathbf{y},\tau)\cdot\,\mathrm{d}\mathbf{S}\,\mathrm{d}\tau-\iint_V(\rho\,\boldsymbol{\omega}\wedge\mathbf{v})(\mathbf{y},\tau)\cdot\frac{\partial G}{\partial\mathbf{y}}(\mathbf{x},\mathbf{y},t,\tau)\,\mathrm{d}^3\mathbf{y}\,\mathrm{d}\tau +\eta\int\oint_S\boldsymbol{\omega}(\mathbf{y},\tau)\wedge\frac{\partial G}{\partial\mathbf{y}}(\mathbf{x},\mathbf{y},t,\tau)\cdot\mathrm{d}\mathbf{S}\,\mathrm{d}\tau, \tag{19}$$

where $\rho_o B(\mathbf{x},t)\approx p(\mathbf{x},t)$ in the linear acoustic region, far from the sources.

The surface integral involving the normal component of $\partial\mathbf{v}/\partial\tau$ determines the influence of surface motions and is nominally equivalent to a distribution of monopole sources on S. The volume integral represents the sound generated by vortex sources within the fluid, taking account of the surface S, whose presence determines the functional form of $G(\mathbf{x},\mathbf{y},t,\tau)$. The final integral supplies the contribution from frictional forces on S.

3. Sound produced by a compact body in arbitrary, deformable motion

3.1. Compact Green's function

In an important class of practical problems the flow Mach number is small, the fluid can be regarded to be in a mean state of rest at large distances from the boundary S, and S or some prominent geometrical feature of S, is acoustically compact, that is, small compared to the wavelength of sound produced by the motion. The production of sound is then governed by Eq. (6) with solution (19) in which ρ in the integrands can be replaced by the mean density ρ_o. For a rigid surface S the dominant source is then of dipole type and the sound can be computed from Eq. (19) by replacing $G(\mathbf{x},\mathbf{y},t,\tau)$ by its *compact* approximation [6,7,24]. But the compact Green's function is also applicable when the surface S is in *arbitrary* low Mach number motion, involving changes in the shape and interior volume with time. In such cases there is usually a monopole component of the sound, and the compact Green's function provides the solution correct to terms of monopole and dipole order in a formal multipole expansion of the full solution. It is given by Howe [6,7,24]:

$$G(\mathbf{x},\mathbf{y},t,\tau)=\frac{1}{4\pi|\mathbf{X}-\mathbf{Y}|}\,\delta\Big(t-\tau-\frac{|\mathbf{X}-\mathbf{Y}|}{c_o}\Big), \tag{20}$$

where $\mathbf{X}=\mathbf{X}(\mathbf{x},t)$, $\mathbf{Y}=\mathbf{Y}(\mathbf{y},\tau)$ are respectively representations of the Kirchhoff vector for S, defined as in Eq. (12), but now dependent on time because of the motion of S. Representation (20) is applicable provided at least one of the points $\mathbf{x}$, $\mathbf{y}$ lies in the acoustic far field of S.

Eq. (20) is a *formal* expression for the compact Green's function that clearly reduces to the free space Green's function

$$G(\mathbf{x},\mathbf{y},t,\tau)=\frac{1}{4\pi|\mathbf{x}-\mathbf{y}|}\,\delta\left(t-\tau-\frac{|\mathbf{x}-\mathbf{y}|}{c_o}\right), \tag{21}$$

which determines solution (10) of Eq. (6) (i.e. of the low Mach number form of Eq. (3)) when the flow is unbounded, when $\mathbf{X}$ and $\mathbf{Y}$ reduce, respectively, to $\mathbf{x}$ and $\mathbf{y}$. However, in applications it is necessary to expand Eq. (20) correctly to dipole order to furnish explicit predictions. By taking the origin O within S, the source point $\mathbf{y}$ near S and the observation point $\mathbf{x}$ in the acoustic far field where $|\mathbf{X}|\approx|\mathbf{x}|\gg|\mathbf{Y}|$, we accordingly obtain the expansion of Eq. (20) to be

$$G(\mathbf{x},\mathbf{y},t,\tau)\approx\frac{1}{4\pi|\mathbf{x}|}\delta\left(t-\tau-\frac{|\mathbf{x}|}{c_o}\right)+\frac{x_iY_i}{4\pi c_o|\mathbf{x}|^2}\delta'\left(t-\tau-\frac{|\mathbf{x}|}{c_o}\right),\quad |\mathbf{x}|\to\infty, \tag{22}$$

where the prime denotes differentiation with respect to t. The first term in this formula does not depend on the source position $\mathbf{y}$, and determines the monopole component of sound; the second represents the dipole. The question of which of these terms dominates the far field depends on the properties of the source terms in the integrands of Eq. (19).

Thus, when expansion (22) is used in Eq. (19) (wherein ρ is replaced by the low Mach number approximation ρ_o), the result can be cast in the form

$$\begin{aligned}p(\mathbf{x},t)\approx{}&\frac{\rho_o}{4\pi|\mathbf{x}|}\left[\frac{\partial}{\partial t}\oint_S\mathbf{v}\cdot\mathrm{d}\mathbf{S}\right]+\frac{\rho_o x_i}{4\pi c_o|\mathbf{x}|^2}\frac{\partial}{\partial t}\left[\frac{\partial}{\partial t}\oint_S Y_i\mathbf{v}\cdot\mathrm{d}\mathbf{S}-\oint_S\frac{\mathrm{D}Y_i}{\mathrm{D}t}\mathbf{v}\cdot\mathrm{d}\mathbf{S}\right]\\&-\frac{\rho_o x_i}{4\pi c_o|\mathbf{x}|^2}\frac{\partial}{\partial t}\left[\int\boldsymbol{\omega}\wedge\mathbf{v}\cdot\nabla Y_i\,\mathrm{d}^3\mathbf{y}-\nu\oint_S\boldsymbol{\omega}\wedge\nabla Y_i\cdot\mathrm{d}\mathbf{S}(\mathbf{y})\right],\quad |\mathbf{x}|\to\infty,\end{aligned} \tag{23}$$

where $\nu=\eta/\rho_o$. Here we adopt the convention that quantities in square braces [ ] are evaluated at the retarded time $t-|\mathbf{x}|/c_o$.

This approximation is correct to dipole order in a multipole expansion of the far field. The first term on the right represents omnidirectional monopole radiation produced by volumetric pulsations of the body S. The remaining terms are *dipoles* and are nominally smaller by a factor $\sim O(M)$, but they become the dominant part of the acoustic field when the volume of the deforming solid is either constant or changes by only a small amount. Those surface dipoles involving $\mathbf{v}\cdot\mathrm{d}\mathbf{S}$ arise from translational, rotational and deformations in the shape of S. The volume integral of $\boldsymbol{\omega}\wedge\mathbf{v}\cdot\nabla Y_i$ corresponds to the result given previously in Eq. (13) for a stationary, compact body; the final term is the contribution from surface frictional dipoles.

3.2. Rigid body in translational motion

The Kirchhoff vector $\mathbf{Y}$ evaluated on the surface S of a rigid body of volume Δ is independent of the time when S is in translational motion at velocity $\mathbf{U}(t)$, say ($M=U/c_o\ll1$). Then Eq. (23) reduces to

$$p(\mathbf{x},t)\approx\frac{\rho_o x_i}{4\pi c_o|\mathbf{x}|^2}\frac{\partial}{\partial t}\left[\oint_S\frac{\partial U_n}{\partial t}Y_i\,\mathrm{d}S-\int(\boldsymbol{\omega}\wedge\mathbf{v})\cdot\nabla Y_i\,\mathrm{d}^3\mathbf{y}+\nu\oint_S\boldsymbol{\omega}\wedge\nabla Y_i\cdot\mathrm{d}\mathbf{S}\right],\quad |\mathbf{x}|\to\infty, \tag{24}$$

where $U_n=\mathbf{U}\cdot\mathbf{n}$ is the normal component of velocity on S (Fig. 4).

Now

$$\rho_o\oint_S\frac{\partial U_n}{\partial t}Y_i\,\mathrm{d}S=\rho_o\frac{\mathrm{d}U_j}{\mathrm{d}t}\oint_S(n_jy_i-n_j\varphi_i^*)\,\mathrm{d}S=(m_o\delta_{ij}+M_{ij})\frac{\mathrm{d}U_i}{\mathrm{d}t},$$

where $m_o=\rho_o\Delta$ is the mass of fluid displaced by the body, and $M_{ij}=M_{ji}=-\rho_o\oint_S n_i\varphi_j^*\,\mathrm{d}S$ is the added mass tensor of the body [6,7].

Therefore, Eq. (24) becomes the dipole radiation field

$$p(\mathbf{x},t)\approx\frac{x_i}{4\pi c_o|\mathbf{x}|^2}\left[\frac{\mathrm{d}F_i}{\mathrm{d}t}+m_o\frac{\mathrm{d}^2U_i}{\mathrm{d}t^2}\right],\quad |\mathbf{x}|\to\infty, \tag{25}$$

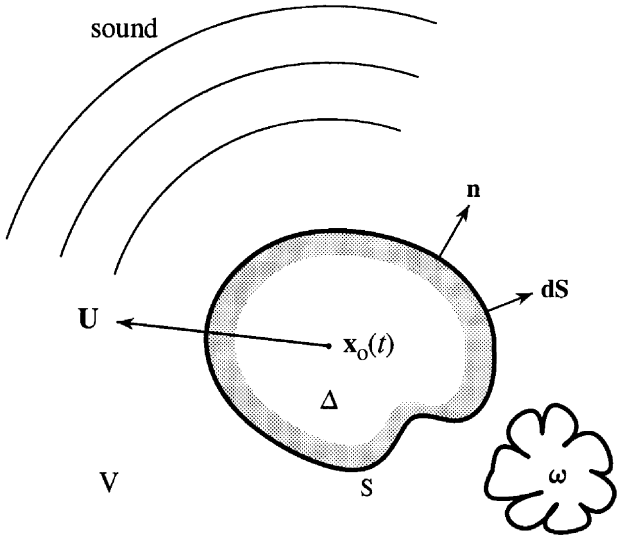

Fig. 4. Compact rigid body in translational accelerated motion.

where

$$F_i = M_{ij}\frac{\mathrm{d}U_j}{\mathrm{d}t} - \rho_o\int_V \boldsymbol{\omega}\wedge\mathbf{v}\cdot\nabla Y_i\,\mathrm{d}^3\mathbf{y} + \eta\oint_S \boldsymbol{\omega}\wedge\nabla Y_i\cdot\,\mathrm{d}\mathbf{S} \tag{26}$$

is the unsteady force exerted on the fluid by the body [6,7].

The result (25) was first obtained by Curle [12] from Lighthill's equation. The force formula (26) gives separate contributions to the unsteady force. The first term, involving the added mass, is independent of the presence of vorticity and depends only on the accelerated motion of S. The contribution from the volume integral containing the Lamb vector $\boldsymbol{\omega}\wedge\mathbf{v}$ corresponds to that already given in Eq. (13) for a stationary rigid body, which is the leading vortex source term at high Reynolds numbers, when the final surface integral in Eq. (26) (which involves the contribution to the force from viscous-induced tangential and normal stresses on S) is negligible.

3.3. Sound produced by a disk of time-dependent radius — Coanda edge-force radiation

Consider a rigid disk of infinitesimal thickness of variable radius $a = a(t)$ placed broadside-on to a uniform, low Mach number mean stream of constant speed U. Dipole sound will be produced by vortex shedding from the disk, but there is no contribution from volumetric or translational motions, both of which are absent. However, the mechanism of sound production shares many similarities with that of *voiced speech* considered later. Let us examine the influence of the variable radius on sound generation by confining attention to the case of an ideal fluid where vortex shedding does not occur and the mean flow is irrotational.

Take the coordinate origin at the fixed centre of the disk, with the x_1 axis normal to the disk and in the direction of the mean flow (Fig. 5). The velocity of the mean flow is $U\nabla X_1(\mathbf{x},t)$, where X_1 is the x_1 component of the Kirchhoff vector, which is defined relative to the coordinates of Fig. 5 by

$$X_1 = x_1 + \frac{2a\,\mathrm{sgn}(x_1)}{\pi}\int_0^\infty\left(\frac{\sin(\xi a)}{\xi a} - \cos(\xi a)\right)\frac{\mathrm{e}^{-\xi|x_1|}J_0(\xi r)\,\mathrm{d}\xi}{\xi}, \quad r = \sqrt{x_2^2 + x_3^2},$$

$$X_2 = x_2, \quad X_3 = x_3, \tag{27}$$

where $a = a(t)$ and J_0 is a Bessel function of order zero.

Provided the frequency of the changes in the radius are such that the disk is acoustically compact, we can use the general formula (23) to calculate the sound produced by the variations in disk radius. The volume of

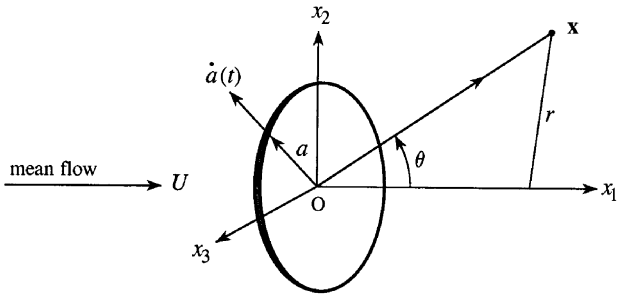

Fig. 5. Generation of sound by a disk of variable radius $a(t)$ placed broadside-on to a uniform, irrotational mean flow.

the disk always vanishes, $\boldsymbol{\omega} = \mathbf{0}$, and the motion is inviscid. Therefore only the first two surface integrals in the dipole term of Eq. (23) can possibly contribute to sound. But the normal component of velocity vanishes on the front and back faces of the disk (where $\mathbf{v} \cdot \mathrm{d}\mathbf{S} \equiv 0$). This implies that any nontrivial contribution to the integrals can only arise because of the known singular behaviour of the potential flow velocity at the edge of the disk, which produces the suction force required to turn the flow around the sharp corner — a 'Coanda effect'. It is the rate of working of the unsteady part of this Coanda edge force that is responsible for the generation of sound.

Near the edge of the disk, Eq. (27) implies that

$$Y_1 \sim \frac{2\sqrt{2a}}{\pi}\,\mathrm{Re}(\mathrm{e}^{\mathrm{i}\pi/4}\sqrt{z-\mathrm{i}a}), \quad z \sim \mathrm{i}a, \quad z = y_1 + \mathrm{i}\sqrt{y_2^2 + y_3^2}, \tag{28}$$

so that $(\nabla Y_1)^2 \sim O(1/|z-\mathrm{i}a|)$ near the edge. It follows that any sound produced by edge effects must be given by the following component of Eq. (23):

$$p(\mathbf{x},t) \approx -\frac{\rho_o x_i}{4\pi c_o |\mathbf{x}|^2}\frac{\partial}{\partial t}\left[\oint_S \frac{\mathrm{D}Y_i}{\mathrm{D}t}\,\mathbf{v}\cdot\mathrm{d}\mathbf{S}\right] = -\frac{\rho_o x_1}{4\pi c_o |\mathbf{x}|^2}\frac{\partial}{\partial t}\left[\oint_S U(\nabla Y_1)^2\mathbf{v}\cdot\mathrm{d}\mathbf{S}\right]. \tag{29}$$

The entire contribution to the last integral is from the neighbourhood of the edge, where the normal component of velocity is $\mathbf{v}\cdot\mathbf{n} = \dot{a}(t) = \mathrm{d}a/\mathrm{d}t$. It can be evaluated using the limiting behaviour (28) by the method described by Batchelor [25, Eq. 6.5.4] for calculating suction force at a sharp edge, which yields

$$p(\mathbf{x},t) \approx -\frac{2\rho_o M\cos\theta}{3\pi|\mathbf{x}|}\left[\frac{\mathrm{d}^2}{\mathrm{d}t^2}(a^3)\right]_{t-|\mathbf{x}|/c_o}, \quad |\mathbf{x}| \to \infty, \tag{30}$$

where θ is the angle shown in Fig. 5 between the radiation direction and the positive x_1-axis. This is a characteristic dipole field whose amplitude and frequency are determined by the time rate of change of the disk radius. The dipole axis is in the mean flow direction, and in fact the dipole strength, is just equal to the amplitude of the unsteady drag force experienced by the disk because of the changes in radius. Observe that there is no requirement that the overall amplitude of the radial variations should be small, although the frequency should be small enough to ensure that the disk remains acoustically compact.

3.4. *Influence of induced vortex shedding: the Kutta condition*

In a typical low Mach number, turbulence–structure interaction a coherent region of vorticity (a 'gust') is swept past a stationary body S in a nominally steady flow. The 'no-slip' condition on S results in the release of additional vorticity into a turbulent wake. For the example in Fig. 6 of a thin rectangular airfoil, the vorticity is shed into a thin wake from the trailing edge. In an approximation where viscosity is neglected, the strength of the shed vorticity is determined by the *Kutta* condition that potential flow singularities in the velocity and pressure at the edge should be absent [26].

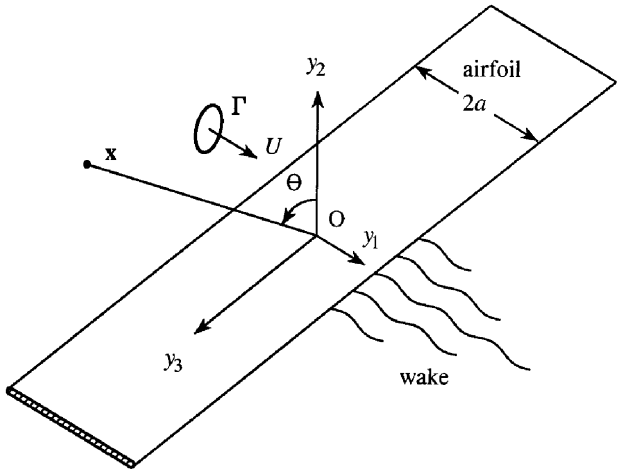

Fig. 6. Sound generation by a vortex ring interacting with an airfoil, including the contribution from the induced vortex wake shed from the trailing edge.

At high Reynolds number the surface force (26) responsible for the sound reduces to

$$F_i = -\rho_o \int_V (\boldsymbol{\omega} \wedge \mathbf{v})(\mathbf{y}, t) \cdot \nabla Y_i(\mathbf{y})\, \mathrm{d}^3\mathbf{y}, \tag{31}$$

where ∇Y_i represents the velocity of an ideal flow past the airfoil that has unit speed in the i-direction at large distances from the airfoil. It is singular (or very large) at the edges of the airfoil. These singularities have the following significance: when the vorticity length scale is small compared to the airfoil chord, the principal contribution to the integral is from vorticity in the neighbourhoods of the singularities. Thus for the airfoil of Fig. 6

$$(Y_1,\ Y_2,\ Y_3) = (y_1,\ \mathrm{Re}\{-\mathrm{i}\sqrt{z^2 - a^2}\},\ y_3), \quad z = y_1 + \mathrm{i}y_2,$$

where ∇Y_2 is infinite at the leading and trailing edges $z = \mp a$. A small-scale gust convecting past the airfoil in the y_1-direction at speed U induces vortex shedding from the trailing edge $z = a$. When this shedding is ignored, the force calculated from (31) has two principal components, namely from gust elements near the leading and trailing edges. To calculate the overall force, however, it is necessary to include the contribution from the shed vorticity, which affects the motion only near the trailing edge when the length scale of the wake vorticity is small. In a linearized treatment of this problem [7,27], when the gust and wake vorticity are both assumed to convect at the *same* mean velocity, it is known from unsteady aerodynamics that the force component produced by the wake is equal and opposite to that generated by the gust at the trailing edge.

The effect of this cancellation on sound can be approximated without calculating any details of shed vorticity, by formally deleting the trailing edge singularity from ∇Y_2 and ignoring the contribution to the integral (31) from shed vorticity. This is because the value of the integral is dominated by vorticity near the edges, and only the behaviours of Y_2 near these edges must be retained in the integrand; Y_2 can therefore be replaced by the leading-order terms in its expansions about the edges. For the airfoil of Fig. 6 one writes

$$Y_2 = \mathrm{Re}(-\mathrm{i}\sqrt{z-a}\sqrt{z+a}) \sim \mathrm{Re}(\sqrt{2a}\sqrt{z+a}) + \mathrm{Re}(-\mathrm{i}\sqrt{2a}\sqrt{z-a}). \tag{32}$$

The last term is singular at the trailing edge. The Kutta condition is imposed by deleting this term, ignoring the wake vorticity and using the following approximation in Eq. (31):

$$Y_2 \sim \mathrm{Re}(\sqrt{2a}\sqrt{z+a}), \tag{33}$$

where the branch cut for $\sqrt{z+a}$ is taken along the real axis from $z = -a$ to $+\infty$.

To illustrate this, consider an idealized gust in the form of a vortex ring of circulation Γ, radius $R \ll a$ and of infinitesimal core. Let the ring be orientated with its normal in the x_1-direction and translate at approximately constant speed U parallel to the airfoil at distance $h > 0$ above the airfoil, such that its centre is at $(Ut, h, 0)$ at time t. If we also assume that $R \ll h$, the gust noise source is equivalent to the quadrupole

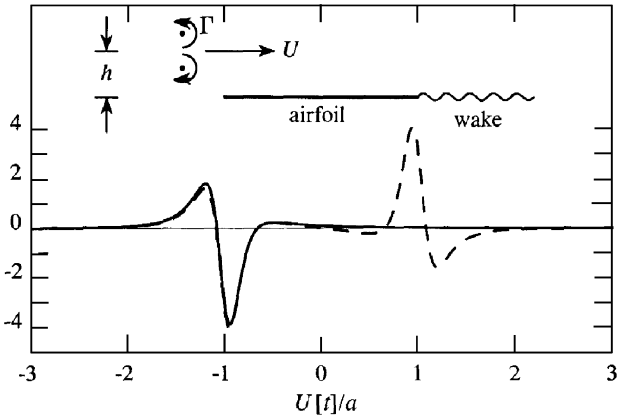

Fig. 7. Nondimensional acoustic pressure (——)

$$p(\mathbf{x},t)\Big/\left(\frac{R}{a}\right)^2\frac{\rho_o U^2\Gamma\cos\Theta}{c_o|\mathbf{x}|}$$

produced by the vortex ring of Fig. 6 when the Kutta condition is imposed and $h/a=0.25$; – – – pressure in the absence of vortex shedding.

$\mathrm{div}(\boldsymbol{\omega}\wedge\mathbf{v})\equiv\partial/\partial x_\alpha(\boldsymbol{\omega}\wedge\mathbf{v})_\alpha$, where the repeated suffix α is summed over $\alpha=2$, 3 only, and

$$(\boldsymbol{\omega}\wedge\mathbf{v})_\alpha=-\pi R^2\Gamma U\,\frac{\partial}{\partial x_\alpha}(\delta(x_1-Ut)\delta(x_2-h)\delta(x_3)).$$

Then Eq. (23) yields, when the Kutta condition is applied at the trailing edge,

$$\begin{aligned}p(\mathbf{x},t)&\approx-\frac{\rho_o\cos\Theta}{4\pi c_o|\mathbf{x}|}\frac{\partial}{\partial t}\left[\int(\boldsymbol{\omega}\wedge\mathbf{v})_\alpha\frac{\partial Y_2}{\partial y_\alpha}\,\mathrm{d}^3\mathbf{y}\right]\\&\approx-\frac{\rho_o\sqrt{2a}\cos\Theta}{4\pi c_o|\mathbf{x}|}\frac{\partial}{\partial t}\left[\int(\boldsymbol{\omega}\wedge\mathbf{v})_\alpha\frac{\partial}{\partial y_\alpha}\,\mathrm{Re}(\sqrt{y_1+\mathrm{i}y_2+a})\,\mathrm{d}^3\mathbf{y}\right]\\&=\frac{3}{16\sqrt{2}}\left(\frac{R}{a}\right)^2\frac{\rho_o U^2\Gamma\cos\Theta}{c_o|\mathbf{x}|}\,\mathrm{Re}\left\{\frac{1}{\left(\dfrac{U[t]}{a}+1+\dfrac{\mathrm{i}h}{a}\right)^{5/2}}\right\},\quad|\mathbf{x}|\to\infty,\end{aligned}\tag{34}$$

where Θ is the angle between the radiation direction $\mathbf{x}$ and the normal to the airfoil (Fig. 6).

The radiation has the characteristic dipole directivity of a compact vortex–surface interaction, the dipole axis being normal to the airfoil, and its magnitude being proportional to the unsteady lift produced by the passing vortex. The pressure signature (34) is plotted as the solid curve of Fig. 7 for the case $h/a=0.25$. The broken line curve is the pressure field generated by the vortex ring near the trailing edge when the Kutta condition is not imposed; this is equal and opposite to the pressure radiated by the wake vorticity.

4. Voiced speech

4.1. Theoretical model

Voiced speech is produced by oscillations of the vocal folds subjected to a nominally steady 'subglottal' pressure from the lungs. Periodic shedding from the 'tips' of the folds and feedback from convecting vorticity produce self-sustaining oscillations of the folds at frequencies f_o, typically ~100–200 Hz for adult speakers [28–30]. In all such cases the glottis (the opening of variable width between the folds) is acoustically compact. An idealized representation (adapted from Ref. [31]) of the fold motion during a complete cycle is shown in

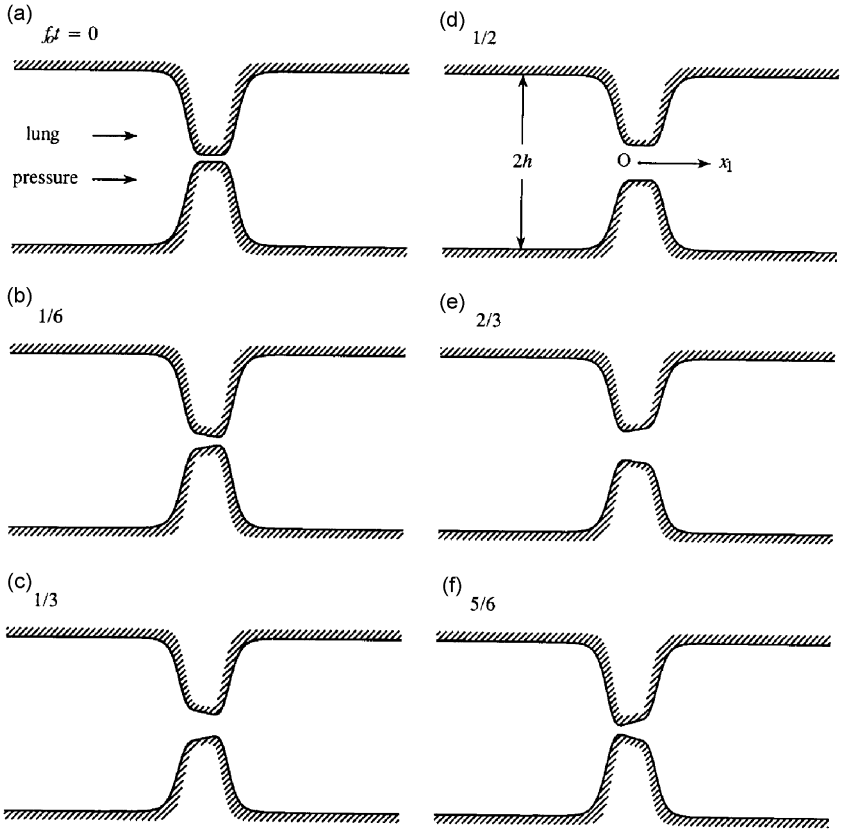

Fig. 8. Illustrating the variations in the geometry of the vocal folds over one cycle at intervals of $\frac{1}{6}$ of a period according to the model of Zhao et al. [31].

Fig. 8. In the simplest approximation, the glottis has a rectangular cross-section of span ℓ_3 (out of the plane of the paper in Fig. 8) and a continuously variable width $\Delta(x_1, t)$, where the origin is at the nominal centroid of the glottis at O with x_1 measured axially with respect to the vocal tract (see Fig. 8d). To obtain a mathematical model of the mechanism of sound production, the vocal tract near the glottis will be treated as a rigid-walled, rectangular duct of span ℓ_3 and height $2h$.

Voicing is typically initiated with the glottis tightly closed and subject to a subglottal over-pressure of about 10 cm of water ($\sim$1 kPa), which blows the folds apart. This is modelled theoretically by the arrival of a step pressure rise from the lungs (from the left in Fig. 8), causing the folds to separate and opening the glottis, initially forming a converging channel as indicated in Fig. 8b. The subsequent 'rocking' motion illustrated in Figs. 8c–f is attributed to structural waves moving over the surfaces ('epithelia') of the folds [30]. A constant applied over-pressure causes the sequence of configurations in Fig. 8 to repeat periodically. The actual variation of $\Delta(x_1, t)$ is determined by the simultaneous solution of equations of motion for the fluid and for the elastic vocal folds.

Let the over-pressure from the lungs consist of a step rise in pressure of amplitude p_I arriving at the glottis at $t = 0$ as the incident wave $B_I = (p_I/\rho_o)H(t - x_1/c_o)$. Then $B = B_I + B_s$, where $B_s = p_s/\rho_o$ is 'scattered' from the glottis with outgoing wave behaviour. A simple modification of the argument leading to Eq. (19) then supplies the acoustic pressure in the form

$$\frac{p}{\rho_o} = \frac{p_I}{\rho_o} H\left(t - \frac{x_1}{c_o}\right) - \int_V (\boldsymbol{\omega} \wedge \mathbf{v})_j(\mathbf{y}, \tau) \frac{\partial G}{\partial y_j}(\mathbf{x}, \mathbf{y}, t, \tau)\, \mathrm{d}^3\mathbf{y}\, \mathrm{d}\tau$$
$$+ \nu \oint_S \boldsymbol{\omega}(\mathbf{y}, \tau) \wedge \frac{\partial G}{\partial \mathbf{y}}(\mathbf{x}, \mathbf{y}, t, \tau) \cdot \mathrm{d}\mathbf{S}(\mathbf{y})\, \mathrm{d}\tau + \oint_S G(\mathbf{x}, \mathbf{y}, t, \tau) \left(\frac{\partial v_j}{\partial \tau} + \frac{\partial B_I}{\partial y_j}\right)(\mathbf{y}, \tau)\, \mathrm{d}S_j(\mathbf{y})\, \mathrm{d}\tau. \quad (35)$$

The compact Green's function for this problem of sound generation in a uniform duct, when the source point at $\mathbf{y}$ is in the vicinity of a deformable contraction (the glottis), can be cast in the form [32]

$$G(\mathbf{x},\mathbf{y},t,\tau)\approx\frac{c_o}{2\mathscr{A}}\,H([t]-\tau)+\frac{c_o\,\mathrm{sgn}(x_1)\,Y_1(\mathbf{y},\tau)}{\ell([t])\mathscr{A}}\,H([t]-\tau)\,\mathrm{e}^{-\int_\tau^{[t]}2c_o\,\mathrm{d}\xi/\ell(\xi)},\quad \mathbf{y}\sim O(h), \tag{36}$$

where $[t]=t-|x_1|/c_o$ is the retarded time, $\mathscr{A}=2h\ell_3$ is the cross-sectional area of the duct and $Y_1(\mathbf{y},\tau)$ is the one-dimensional Kirchhoff vector defined by the potential of flow through the glottis with vanishing normal derivative on the sidewalls. This approximation ignores reflections of sound waves from the distant extremities of the vocal tract, and therefore is limited in its use to the determination of the acoustic field immediately after its generation at the glottis. The length $\ell=\ell(t)$ is an 'end-correction' defined by

$$\ell(t)=\int_{-\infty}^{\infty}\left(\frac{\partial Y_1}{\partial y_1}(\mathbf{y},t)-1\right)\mathrm{d}y_1, \tag{37}$$

where the integration is along any path parallel to the duct axis passing through the contraction, and Y_1 can be normalized such that

$$Y_1\sim y_1\pm\frac{\ell(t)}{2},\quad y_1\to\pm\infty. \tag{38}$$

The end-correction ℓ typically exceeds the duct width $2h$, and becomes very large when the minimum distance between the opposite walls of the contraction is small. Its variation over a complete cycle $0<t<1/f_0$ is illustrated in Fig. 9 for the case where the minimum and maximum widths of the glottis are, respectively, equal to 0.5% and 20% of the duct width $2h$. The exponential function in the second term of Eq. (36) decreases rapidly when the acoustic travel distance $c_o([t]-\tau)$ exceeds ℓ, which provides a time scale for acoustically compact transients. In many applications, however, transients are unimportant because a typical compact source near the contraction does not change over times $\sim\ell/c_o$, and we can then use the more usual approximation

$$G(\mathbf{x},\mathbf{y},t,\tau)\approx\frac{c_o}{2\mathscr{A}}\,H\left(t-\tau-\frac{|X_1-Y_1|}{c_o}\right). \tag{39}$$

4.2. Vortex sound

Irrotational, transient motions dominate the sound radiated from the glottis immediately after the arrival of the step wave, and are governed by the contribution from $\partial B_I/\partial y_j$ in Eq. (35). These integrals in Eq. (35) involving vorticity and surface accelerations are initially small because, for example, vorticity must first be convected into the flow after shedding from the folds by the low Mach number glottal flow. At later times the

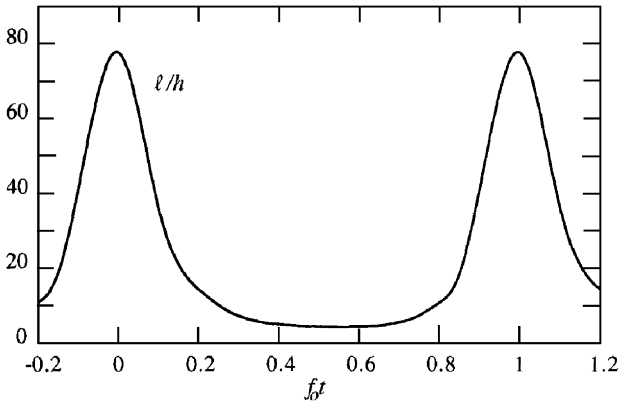

Fig. 9. Variation of the end-correction $\ell(t)$ during periodic motion of the model glottis of Fig. 8 when the minimum and maximum widths of the glottis (corresponding to Figs. 8a, d) are, respectively, 0.5% and 20% of the duct width $2h$.

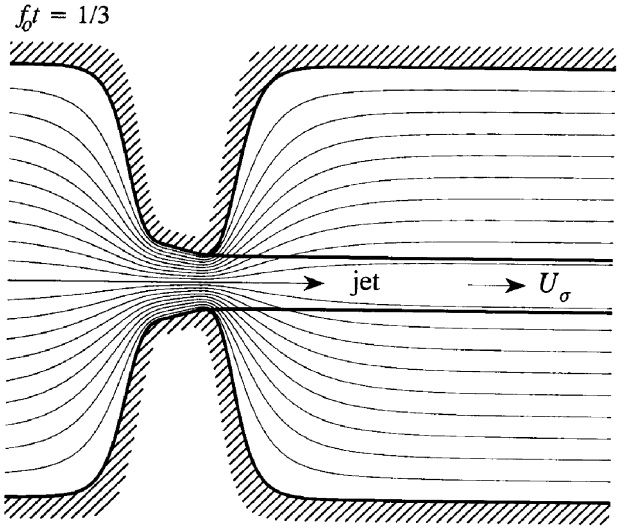

Fig. 10. Glottal jet modelled as a quasi-static free-streamline flow with asymptotic jet speed U_σ at stage (c) of Fig. 8. The majority of the 'streamlines' of Green's function velocity potential $Y_1(\mathbf{x}, t)$ cut the jet boundary typically within a distance downstream of the glottis of the order of the glottal width.

flow just downstream of the glottis forms a jet of rectangular cross-section and span ℓ_3 whose width is modulated by the varying width of the glottis (Fig. 10). The jet is unstable and further downstream the flow becomes turbulent, but is sufficiently far from the glottis that the efficiency of sound production by the turbulence is negligible. Indeed, the vortex sound $B_\omega = p_\omega/\rho_o$, say, is determined by the first integral of Eq. (35) in the form

$$\frac{p_\omega}{\rho_o} = -\int (\boldsymbol{\omega}\wedge\mathbf{v})_j(\mathbf{y},\tau)\,\frac{\partial G}{\partial y_j}(\mathbf{x},\mathbf{y},t,\tau)\,\mathrm{d}^3\mathbf{y}\,\mathrm{d}\tau$$
$$\approx -\frac{c_o\,\mathrm{sgn}(x_1)}{\mathscr{A}\ell([t])}\int_{-\infty}^{[t]} \mathrm{e}^{-\int_\tau^{[t]} 2c_o\,\mathrm{d}\xi/\ell(\xi)}\,\mathrm{d}\tau\int\left(\frac{\partial Y_1}{\partial\mathbf{y}}\cdot\boldsymbol{\omega}\wedge\mathbf{v}\right)(\mathbf{y},\tau)\,\mathrm{d}^3\mathbf{y}. \tag{40}$$

In Fig. 10 the jet and streamline patterns of the 'flow' defined by the velocity potential Y_1 are shown at stage (c) of Fig. 8. Sound is generated strongly (with dipole strength) in regions where the streamline pattern of Y_1 varies rapidly, on scales comparable to those of the vortex field. This occurs close to the glottis within a distance $\sim$ the glottal width — further downstream the streamlines are uniformly spaced, parallel and ∇Y_1 varies very slowly, and the integration in Eq. (40) can then be evaluated by holding $\partial Y_1/\partial\mathbf{y}$ constant over the region occupied by a coherent eddy, in which case $\int\boldsymbol{\omega}\wedge\mathbf{v}\,\mathrm{d}^3\mathbf{y} = 0$ when the eddy is compact: under these circumstances the sound generated by the eddy is that of a weak quadrupole.

Fig. 10 also illustrates the consequence of the high Reynolds number hypothesis that vorticity shed from the glottis is initially confined to 'free streamlines' at the edges of the jet. From what has been said above, it is only necessary for this approximation to be adequate within a distance of about one glottal width downstream, where Green's function streamlines of the potential Y_1 *cut across* the jet boundary. On this boundary the flow speed is constant and equal to U_σ, say, the asymptotic jet velocity predicted by the free-streamline theory [33,34]. Thus, for example, along the upper free streamline of Fig. 10 the vorticity $\boldsymbol{\omega} = U_\sigma\delta(s_\perp)\mathbf{k}$, where $s_\perp$ is the distance measured in the direction of the outward normal from the free streamline and $\mathbf{k}$ is a unit vector out of the plane of the paper; the vorticity convection velocity $\mathbf{v} = \frac{1}{2}U_\sigma\mathbf{t}$, where $\mathbf{t}$ is a unit vector tangential to the free-streamline flow. Hence, because $\mathbf{k}\wedge\mathbf{t}$ is the unit normal directed outwards from the jet, the contributions from both edges of the jet can be combined to yield

$$\int\left(\frac{\partial Y_1}{\partial\mathbf{y}}\cdot\boldsymbol{\omega}\wedge\mathbf{v}\right)(\mathbf{y},\tau)\,\mathrm{d}^3\mathbf{y} = \ell_3 U_\sigma^2(\tau)\int_0^\infty\left(\frac{\partial Y_1}{\partial s_\perp}\right)_{s_\perp=0}\mathrm{d}s,$$

where s is the distance measured along a free streamline from the glottis. Now $2\ell_3\int_0^\infty(\partial Y_1/\partial s_\perp)_{s_\perp=0}\,\mathrm{d}s=\mathscr{A}$, provided the asymptotic jet width is small compared to the width $2h$ of the vocal tract. Therefore the vortex sound formula (40) becomes

$$\frac{p_\omega}{\rho_o}\approx-\frac{c_o\,\mathrm{sgn}(x_1)}{2\ell([t])}\int_{-\infty}^{[t]}U_\sigma^2(\tau)\mathrm{e}^{-\int_\tau^{[t]}2c_o\,\mathrm{d}\xi/\ell(\xi)}\,\mathrm{d}\tau. \tag{41}$$

4.3. Solution of the scattering problem

The remaining integrals in Eq. (35) include the contribution from the incident step wave (the term in $\partial B_I/\partial y_j$), which is readily evaluated in the form

$$-\frac{p_I}{\rho_o}\frac{\mathrm{sgn}(x_1)}{\ell([t])}\int_{-\infty}^{[t]}\frac{\partial}{\partial\tau}\,(H(\tau)\ell(\tau))\mathrm{e}^{-\int_\tau^{[t]}2c_o\,\mathrm{d}\xi/\ell(\xi)}\,\mathrm{d}\tau,$$

and represents a transient response to the incident step rise in pressure. It decays rapidly to zero after a retarded time $\sim\ell/c_o$, where ℓ is the characteristic value of the glottis end-correction following its impulsive opening.

In addition, there are contributions from the frictional, viscous drag in the glottis and from the cyclic variations in the *volume* of the vocal folds. The viscous term will be neglected — it is significant only when $\Delta\to0$, but it can still be ignored because the end-correction $\ell\to\infty$ as the glottis closes, causing the overall radiation to drop to zero. The periodic changes in vocal fold volume give rise to a small monopole component p_m of the pressure that radiates equal waveforms in both directions away from the glottis:

$$\frac{p_m}{\rho_o}\approx-\frac{c_o\ell_3}{2\mathscr{A}}\frac{\partial}{\partial t}\int_{-\infty}^{\infty}\Delta\left(y_1,t-\frac{|x_1|}{c_o}\right)\mathrm{d}y_1. \tag{42}$$

Hence, combining these pressures with the vortex sound component (41) the solution (35) becomes

$$\begin{aligned}p(x_1,t)=p_I\Bigg\{H\left(t-\frac{x_1}{c_o}\right)&-\frac{\mathrm{sgn}(x_1)}{\ell([t])}\int_{-\infty}^{[t]}\frac{\partial}{\partial\tau}\,(H(\tau)\ell(\tau))\mathrm{e}^{-\int_\tau^{[t]}2c_o\,\mathrm{d}\xi/\ell(\xi)}\,\mathrm{d}\tau\Bigg\}\\&-\frac{\rho_oc_o\,\mathrm{sgn}(x_1)}{2\ell([t])}\int_{-\infty}^{[t]}U_\sigma^2(\tau)\mathrm{e}^{-\int_\tau^{[t]}2c_o\,\mathrm{d}\xi/\ell(\xi)}\,\mathrm{d}\tau-\frac{\rho_oc_o\ell_3}{2\mathscr{A}}\frac{\partial}{\partial t}\int_{-\infty}^{\infty}\Delta(y_1,[t])\,\mathrm{d}y_1,\\&\text{where }[t]=t-\frac{|x_1|}{c_o}.\end{aligned} \tag{43}$$

4.4. The voiced pressure signature

The monopole contribution (42) to the radiated sound (43) is readily evaluated when the time dependence of the vocal fold shape function is known. Denote the remaining pressure in Eq. (43) by

$$\begin{aligned}p'(x_1,t)=p_I\Bigg\{H\left(t-\frac{x_1}{c_o}\right)&-\frac{\mathrm{sgn}(x_1)}{\ell([t])}\int_{-\infty}^{[t]}\frac{\partial}{\partial\tau}(H(\tau)\ell(\tau))\mathrm{e}^{-\int_\tau^{[t]}2c_o\,\mathrm{d}\xi/\ell(\xi)}\,\mathrm{d}\tau\Bigg\}\\&-\frac{\rho_oc_o\,\mathrm{sgn}(x_1)}{2\ell([t])}\int_{-\infty}^{[t]}U_\sigma^2(\tau)\,\mathrm{e}^{-\int_\tau^{[t]}2c_o\,\mathrm{d}\xi/\ell(\xi)}\,\mathrm{d}\tau.\end{aligned} \tag{44}$$

For $x_1>0$ the acoustic particle velocity of this outgoing wave has the limiting value $U(t)=\lim_{x_1\to+0}p'(x_1,t)/\rho_oc_o$ just to the right of the glottis in Fig. 8 (i.e. where $x_1\sim+0$ so that $[t]\to t$). By differentiating the corresponding limit of Eq. (44) we find that U satisfies the differential equation

$$\frac{\mathrm{d}(\ell U)}{\mathrm{d}t}+2c_oU+\frac{1}{2}U_\sigma^2=\frac{2p_I}{\rho_o}H(t). \tag{45}$$

If σ is the contraction ratio of the glottal jet, then by continuity $\sigma U_\sigma \Delta_m = 2hU$, where $\Delta_m(t)$ is the minimum width of the glottis at time t, and Eq. (45) becomes

$$\frac{\mathrm{d}(\ell U)}{\mathrm{d}t} + 2c_o U + 2\left(\frac{h}{\sigma\Delta_m(t)}\right)^2 U^2 = \frac{2p_I}{\rho_o} H(t). \tag{46}$$

This equation is equivalent to the nonlinear 'lumped-parameter' approximation used to study voicing by Fant [28] and Flanagan [29], where the vocal tract is modelled as an electrical transmission line with a 'monopole' source of strength $Q \equiv U\mathscr{A}$ at the glottis. The monopole interpretation of the source of voiced speech is obviously incorrect, but it does provide a convenient working model that is often useful. The predominantly dipole character of voiced sounds was established by the numerical work of Zhao et al. [31], who showed that the principal source is the fluctuating surface pressures on the vocal folds.

The *causal* solution of Eq. (46) completely determines the acoustic pressure from the formulae

$$p(x_1,t) = \rho_o c_o U\left(t - \frac{x_1}{c_o}\right) - \frac{\rho_o c_o \ell_3}{2\mathscr{A}} \frac{\partial}{\partial t}\int_{-\infty}^{\infty} \Delta\left(y_1, t - \frac{x_1}{c_o}\right) \mathrm{d}y_1, \quad x_1 \to +\infty \tag{47a}$$

$$= p_I\left[H\left(t - \frac{x_1}{c_o}\right) + H\left(t + \frac{x_1}{c_o}\right)\right] - \rho_o c_o U\left(t + \frac{x_1}{c_o}\right) - \frac{\rho_o c_o \ell_3}{2\mathscr{A}} \frac{\partial}{\partial t}\int_{-\infty}^{\infty} \Delta\left(y_1, t + \frac{x_1}{c_o}\right) \mathrm{d}y_1, \quad x_1 \to -\infty. \tag{47b}$$

The first three cycles of the pressure wave radiated towards the mouth ($x_1 > 0$) calculated from Eq. (47a) by numerical integration of Eq. (46) is illustrated in Fig. 11 when the incident step pressure $p_I = 8$ cm of water ($\sim$0.8 kPa). It is assumed that $c_o = 340$ m/s, $\rho_o = 1.23$ kg/m^3, and the simplest approximation has been adopted in which the jet contraction ratio $\sigma = 1$. The frequency $f_o = 125$ Hz, which is typical of an adult male; in one complete cycle the vocal folds are assumed to pass through the stages shown in Fig. 8 with $h = 10$ mm, when the minimum glottal width of Fig. 8a is $D_{\min} = 0.1$ mm and the maximum (Fig. 8d) is $D_{\max} = 4$ mm. Fig. 11 shows the overall predicted waveform (——), a series of positive pulses, and also shows the separate contributions (- - - -) from the vortex sound term $\rho_o c_o U$ of Eq. (47a) (superimposed on the mean transmitted pressure of amplitude p_I) and monopole (42).

It is seen that the rapid transient build-up of the transmitted sound to its periodic form occupies a small fraction of a cycle. The shape of the transient is controlled by the first term on the left of Eq. (46). When this is discarded the equation yields the quasi-static approximation

$$U(t) = \frac{c_o}{2}\frac{\sigma\Delta_m(t)}{h}\left(\sqrt{\left(\frac{\sigma\Delta_m(t)}{h}\right)^2 + \frac{4p_I}{\rho_o c_o^2}} - \frac{\sigma\Delta_m(t)}{h}\right), \quad t > 0. \tag{48}$$

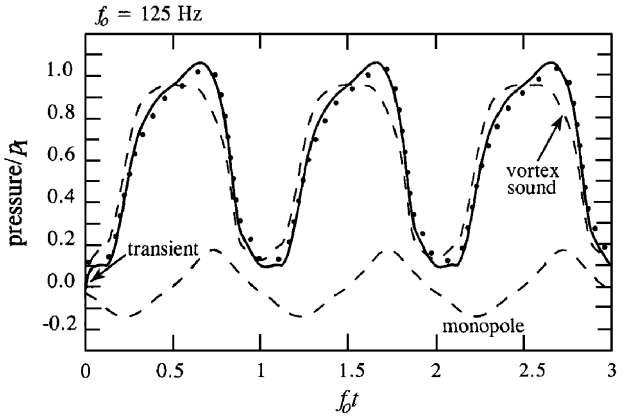

Fig. 11. The first three cycles of the pressure (47a) (——) radiated from the glottis towards the mouth ($x_1 > 0$) when $f_0 = 125$ Hz, $p_I = 8$ cm of water, $D_{\min} = 0.1$ mm. Also shown (- - - -) are the separate contributions from the vortex sound superimposed on the mean transmitted pressure p_I, and the monopole sound (42). The dotted curve (• • •) is the quasi-static approximation (48).

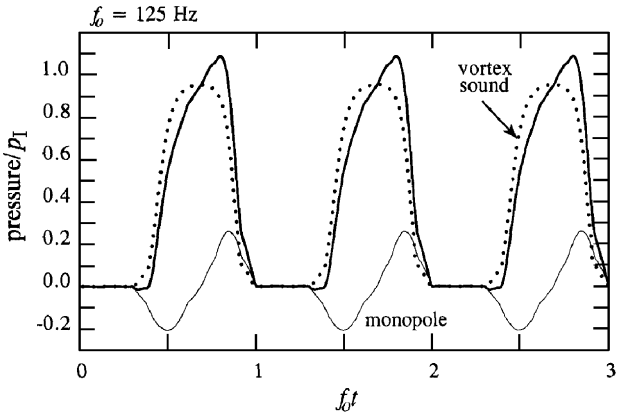

Fig. 12. The quasi-static approximation to the pressure (48) (——) radiated from the glottis towards the mouth ($x_1 > 0$) when $f_0 = 125$ Hz, $p_I = 8$ cm of water, but when the glottis is closed during the first 30% of each cycle, producing a succession of pressure pulses separated by short intervals of 'silence'.

The prediction of sound using this formula in Eq. (47a) is plotted as the dotted curve (• • •) in Fig. 11. Evidently the neglect of the 'inductive' term in Eq. (46) results in a prediction that lacks an initial transient but is otherwise a very close approximation to the full predicted acoustic pressure. The dominant influence of the variable end-correction $\ell(t)$ is confined to the very initial phases of sound generation. The monopole contribution alternates in sign as the folds expand and contract and furnishes a small correction to the overall wave profile. Although the amplitude of this source would be expected to increase with frequency, it actually appears that structural changes in the vocal folds at higher frequencies tend to oppose this increase [30].

The transmitted pressure remains positive and always exceeds about $0.1p_I$, because it has been assumed that the glottis does not close completely. In voiced speech the periodic motions of the vocal folds usually include intervals in which the glottis is closed. This is easily included in the quasi-static approximation, whereas the corresponding change in the connectivity of the three-dimensional space forming the vocal tract would require special treatment of the full Eq. (46), involving a limiting process in which $\ell/h \to \infty$.

Fig. 12 depicts an example where $D_{\min} = 0$ and the glottis is closed for 30% of each cycle and varies as in Fig. 8 during the remainder of the cycle (again for $f_0 = 125$ Hz and $p_I = 8$ cm of water). Successive pressure pulses are now separated by short intervals of 'silence'. The maximum amplitude of the vortex sound is unchanged from that shown in Fig. 11 because the net variation in the glottal area is the same; however, the contribution from the monopole is increased because the volumetric changes of the folds occur more rapidly.

5. Noncompact sources — the high-speed train

A high-speed train entering a tunnel at speed U compresses the air in front, causing most of it to flow over the train and out of the tunnel portal. The pressure rise propagates ahead of the train into the tunnel at the speed of sound as a compression wave whose amplitude ~1–3% of atmospheric pressure when the train Mach number $M = U/c_o$ exceeds about 0.2 (Fig. 13). The initial shape of the wavefront depends on the geometries of the tunnel portal and train nose, and on the 'blockage' $= \mathscr{A}_o/\mathscr{A}$, where $\mathscr{A}_o$ and $\mathscr{A}$ are, respectively, the cross-sectional areas of the train and tunnel (see [20] and references cited therein). The reflection of the compression wave from the distant tunnel exit is accompanied by the emission from the tunnel of a pressure pulse called the *micro-pressure* wave (Fig. 13), whose strength is proportional to the steepness of the compression wavefront at the exit. For tunnels longer than about 3 km with 'acoustically smooth' concrete slab tracks, nonlinear steepening of the compression wave in the tunnel can cause the micro-pressure wave amplitude to be comparable to the sonic boom overpressure from a supersonic aircraft, and strong enough to rattle windows and fittings in neighbouring dwellings.

One method of suppressing the micro-pressure wave involves judicious modifications of the train nose profile and tunnel portal that increase the initial thickness of the wavefront and delay the onset of nonlinear

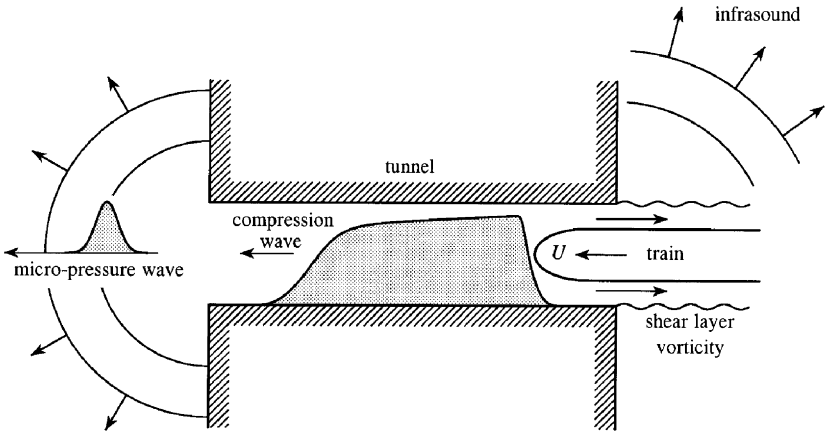

Fig. 13. The compression wave, micro-pressure wave and infrasound generated by a high-speed train entering a tunnel.

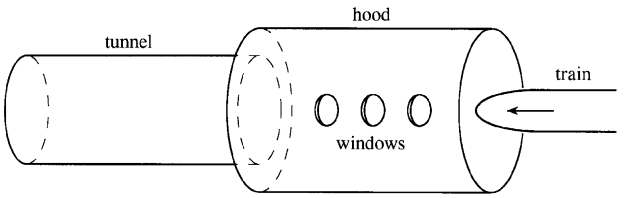

Fig. 14. Schematic scale model experiment involving a train entering an axisymmetric cylindrical tunnel fitted with a tunnel entrance hood with windows.

steepening [35]. Large increases in thickness are achieved by installing a tunnel entrance 'hood' extending up to 50 m out from the tunnel portal. The compression wave begins to form as the train enters the hood: wave thickness increases are obtained by the temporary trapping of wave energy within the hood by multiple reflections from its ends, and by the venting of high-pressure air through 'windows' in the hood walls. The optimization of the hood design is usually based on scale-model testing involving a 'tunnel' consisting of a thin-walled, circular cylindrical tube (of radius $R\sim 50$ mm), and axisymmetric 'trains' projected at high speed into the hood (of radius $R_h \geqslant R$, Fig. 14). The Reynolds number is large enough for the initial interactions of the train and tunnel to be regarded as inviscid, so that model scale experiments should provide a faithful representation of full-scale results, provided the Mach number and relative geometrical sizes of the tunnel and train are the same.

5.1. Basic source mechanism

Coordinates $\mathbf{x} = (x, y, z)$ are taken with the origin O on the axis of symmetry at the hood entrance (Fig. 15). An axisymmetric model scale 'train' is projected into the hood along a guide-wire aligned with the tunnel axis and the compression wave is measured in the tunnel about one metre from the junction of the tunnel and the hood. The circular cross-section of the train becomes uniform with radius h and area $\mathscr{A}_o = \pi h^2$ at a distance L from the train nose.

The production of the compression wave is governed by the vortex sound equation (15). But now there are two important surfaces, the fixed interior and exterior tunnel walls and that of the moving train. For practical purposes it is convenient to use a Green's function having vanishing normal derivative only on the tunnel surface. The effect of the moving train is then contained in the terms

$$\rho \nabla H \cdot \frac{\partial \mathbf{v}}{\partial t} - \nabla \cdot (\rho B \nabla H) \tag{49}$$

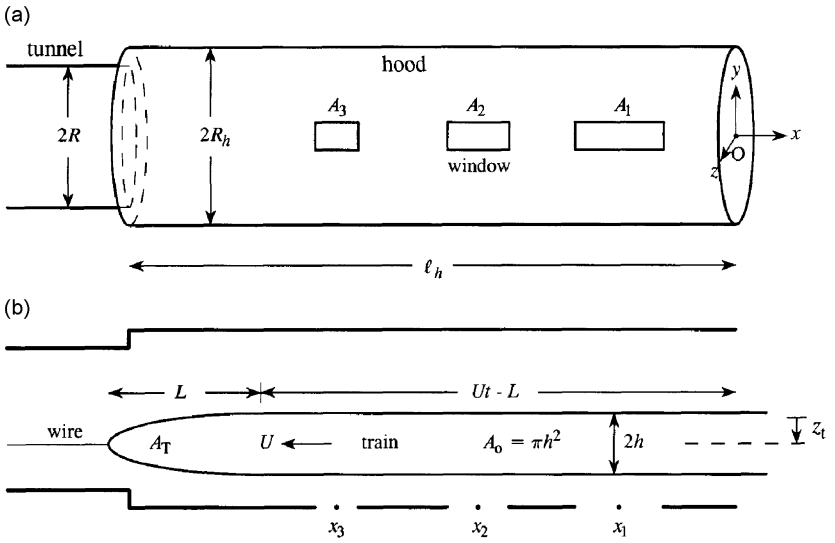

Fig. 15. Experimental hood, tunnel and axisymmetric train: (a) 'side' view from the direction of the positive z-axis; (b) 'top' view from the direction of the positive y-axis.

on the right of Eq. (15), which, respectively, correspond to monopole and dipole sources distributed on the surface of the moving train. The remaining source terms, involving the vorticity, are discussed below.

The monopoles account for the massive displacement of the air ahead of the advancing train. Their interaction with a hood, tunnel or other neighbouring structure produces a pressure excess over the nose of the train (i.e. a *drag* force) that is acoustically equivalent to a distribution of dipoles. Because the blockage $\mathscr{A}_o/\mathscr{A}$ is always small ($\leqslant 0.2$, where $\mathscr{A} = \pi R^2$ = area of the uniform section of the tunnel), the monopole and dipole sources (49) can be replaced by the following slender body approximation [36]:

$$U\left(1+\frac{\mathscr{A}_o}{\mathscr{A}}\right)\frac{\partial}{\partial t}\left(\frac{\partial \mathscr{A}_T}{\partial x}(x+Ut)\delta(y)\delta(z-z_t)\right), \tag{50}$$

where $\mathscr{A}_T(s)$ is the cross-sectional area of the train at distance s from the tip of the nose, which is assumed to enter the hood ($x = 0$) at time $t = 0$ travelling along a guide-wire displaced a distance $z = z_t$ from the tunnel axis. The approximation replaces the surface monopoles and dipoles by a line source on the train axis over the interval of variable train cross-section. The term in Eq. (50) involving the factor $\mathscr{A}_o/\mathscr{A}$ represents the contribution from the drag dipole.

5.2. The compact approximation

In the absence of a hood ($R_h = R$ and no windows in Fig. 15) the experimental train enters a uniform circular cylindrical tube. The train nose interacts with the portal over a time $\sim R/U$ during which the compression wavefront is completely formed with thickness $\sim R/M \gg R$ for typical train Mach numbers $M \sim 0.3$ (370 km/h). We can therefore use the following compact approximation to Green's function [37]:

$$G(\mathbf{x},\mathbf{y},t,\tau) \approx \frac{c_o}{2\mathscr{A}}\left\{H\left(t-\tau-\frac{|\varphi_E^*(\mathbf{x})-\varphi_E^*(\mathbf{y})|}{c_o}\right)-H\left(t-\tau+\frac{\varphi_E^*(\mathbf{x})+\varphi_E^*(\mathbf{y})}{c_o}\right)\right\}, \tag{51}$$

where $\varphi_E^*(\mathbf{x})$ is the velocity potential of a hypothetical incompressible flow *out* of the tunnel portal normalized such that

$$\varphi_E^*(\mathbf{x}) \sim \begin{cases} x-\ell_E & \text{as } x \to -\infty \text{ inside the tunnel,} \\ -\mathscr{A}/4\pi|\mathbf{x}| & \text{as } |\mathbf{x}| \to \infty \text{ outside the tunnel.} \end{cases} \tag{52}$$

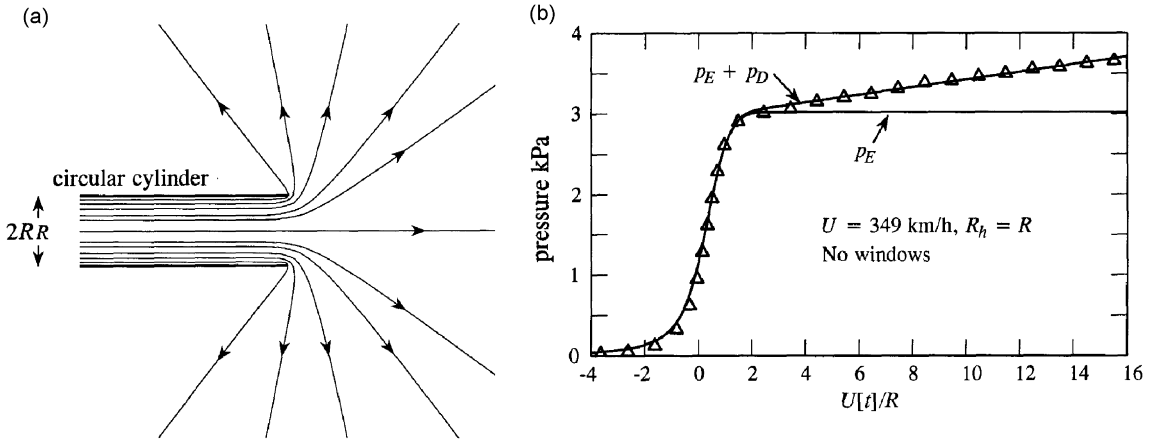

Fig. 16. (a) Streamline pattern of the velocity potential $\varphi_E^*(\mathbf{x})$ defining flow from a circular cylindrical portal. (b) Measured (△) and predicted compression wave in the absence of a hood and windows, for the model scale ellipsoidal nose train defined by Eqs. (57) and (58) and a circular cylindrical tunnel of radius $R = 50$ mm at $U = 349$ km/h when $z_t = 0$. The main pressure rise is determined by p_E of Eq. (53). The linearly increasing 'tail' is governed by the turbulence-generated pressure p_D.

The explicit functional form of $\varphi_E^*(\mathbf{x})$ is given in Ref. [37] for a circular cylindrical portal (and the corresponding pattern of streamlines is shown in Fig. 16a), but the compact approximation (with the appropriate $\varphi_E^*(\mathbf{x})$) is applicable for any tunnel whose interior cross-sectional area is ultimately constant and equal to $\mathscr{A}$. The length ℓ_E is an 'end-correction' determined by the shape of the portal.

Thus ahead of the train within the tunnel where $B = p/\rho_o$, slender body approximation (50) supplies the compression wave in the form

$$p_E(\mathbf{x},t) \approx \rho_o U\left(1+\frac{\mathscr{A}_o}{\mathscr{A}}\right)\frac{\partial}{\partial t}\iint_{-\infty}^{\infty}\frac{\partial \mathscr{A}_T}{\partial x'}(x'+U\tau)G(\mathbf{x},(x',0,z_t),t,\tau)\,\mathrm{d}x'\,\mathrm{d}\tau$$
$$\approx \frac{\rho_o U^2}{\mathscr{A}(1-M^2)}\left(1+\frac{\mathscr{A}_o}{\mathscr{A}}\right)\int_{-\infty}^{\infty}\frac{\partial \mathscr{A}_T}{\partial x'}(x'+U[t])\,\frac{\partial \varphi_E^*}{\partial x'}(x',0,z_t)\,\mathrm{d}x', \tag{53}$$

where $[t] = t + (x-\ell_E)/c_o$ is the effective retarded time, and the subscript 'E' on p_E signifies the component of the overall compression wave pressure attributable to the interaction of the train nose with the portal alone. Because nonlinear propagation terms have been ignored, this approximation determines the *initial* form of the compression wave before the onset of nonlinear steepening. It is therefore applicable within the region several tunnel diameters ahead of the train, during and just after tunnel entry.

To illustrate the roles played by the various terms in the integrand of Eq. (53), consider the limiting case of a 'snub-nosed' train whose nose length $L \to 0$, for which $\mathscr{A}_T(s) = \mathscr{A}_o H(s)$, so that the source distribution (50) representing the train nose collapses to a point source with

$$\frac{\partial \mathscr{A}_T}{\partial x'}(x'+U[t]) = \mathscr{A}_o\delta(x'+U[t]). \tag{54}$$

Then Eq. (53) gives

$$p_E(\mathbf{x},t) \approx \frac{\rho_o U^2}{(1-M^2)}\,\frac{\mathscr{A}_o}{\mathscr{A}}\left(1+\frac{\mathscr{A}_o}{\mathscr{A}}\right)\frac{\partial \varphi_E^*}{\partial x'}\,(-U[t],0,z_t), \tag{55}$$

which shows that in this limiting case the compression wave profile is an exact image of the axial component of the potential flow velocity $\partial\varphi_E^*/\partial x$ along the track of the train. The rapid expansion of the streamline pattern outside the portal (Fig. 16a) indicates that this velocity is very small before the nose enters the tunnel ($\sim\mathscr{A}/4\pi x^2$ when $x > R$), but rises quickly and smoothly to $\partial\varphi_E^*/\partial x = 1$ when $x < -R$ within the tunnel. The rate of increase of pressure across the wavefront is strongly dependent on the relative track offset z_t/R, becoming increasingly fast as z_t increases from zero when the path of the train traverses the rapidly varying

streamline pattern near the edge of the portal. Evidently, the pressure profile for a train nose of finite length will correspond to a 'smeared' image of $\partial\varphi_E^*/\partial x$ along the path of the train.

Eq. (55) shows that the overall pressure rise Δp_E *across the wavefront* is

$$\Delta p_E = \frac{\rho_o U^2}{(1-M^2)}\frac{\mathscr{A}_o}{\mathscr{A}}\left(1+\frac{\mathscr{A}_o}{\mathscr{A}}\right). \tag{56}$$

Actually, this result does not depend on the shape of the train nose because, after the nose has passed into the tunnel, $\partial\varphi_E^*/\partial x' = 1$ in the region occupied by the nose, and the right-hand side of Eq. (53) reduces exactly to this formula.

Fig. 16b depicts the measured compression wave profile ($\triangle\ \triangle\ \triangle$) for a typical laboratory scale test for this case of a tunnel without a hood. The experiment was performed at the Railway Technical Research Institute (RTRI) in Tokyo [20] using apparatus described in Ref. [38]. The tunnel consisted of a 6.5 m-long, thin-walled, circular cylindrical tube of internal radius $R = 50$ mm. The model axisymmetric 'train' had an ellipsoidal nose shape defined by

$$r = h\sqrt{\frac{x}{L}\left(2-\frac{x}{L}\right)}, \quad 0<x<L\ (r=\sqrt{y^2+z^2}), \tag{57}$$

so that (ignoring the rear end of the train)

$$\frac{\mathscr{A}_T(s)}{\mathscr{A}_o} = \begin{cases} \dfrac{s}{L}\left(2-\dfrac{s}{L}\right), & 0<s<L, \\ 1, & s>L, \end{cases} \tag{58}$$

where $h = 22.35$ mm, $L = 67.05$ mm and $\mathscr{A}_o/\mathscr{A} = 0.2$. The tail of the train had an identical ellipsoidal shape, and its overall length was 1239 mm.

The train was projected into the tunnel at $U = 349$ km/h ($M = 0.285$) along the tunnel axis. The front of the nose crosses the entrance plane of the tunnel at $t = 0$, and the pressure wave was measured within the tunnel at a distance $\ell_m = 1.5$ m from the entrance. In the figure the pressure at $x = -\ell_m$ is plotted against $U[t]/R$, where $[t] = t - \ell_m/c_o$ is the retarded time. The pressure rise begins just before the nose enters the tunnel at $U[t]/R = 0$. The calculated pressure rise p_E generated by the interaction of the nose with the tunnel entrance is seen to agree with the principal characteristics of the measured wavefront, but assumes the constant value given by Eq. (56) for $U[t]/R > 2$. The subsequent linear increase in the measured pressure is caused by the frictional drag on the train and tunnel walls, and will be discussed below.

5.3. *Influence of aerodynamic drag*

The principal interactions that contribute to compression wave formation are illustrated in Fig. 17 for a generic hood with *one* window. The influences of windows (W) and of the junction J between the tunnel and hood are discussed later. For the moment we confine attention to the problem discussed in Section 5.2 (no hood and no windows, $R_h = R$) and examine how the calculated wavefront pressure p_E is augmented by frictional forces that generate an additional pressure p_D responsible for the gradual and practically linear increase in the measured pressure to the rear of the main pressure rise in Fig. 16. This pressure is produced by the vortex sources

$$\nabla\cdot(H\rho\,\boldsymbol{\omega}\wedge\mathbf{v}) + \eta\nabla\cdot(\nabla H\wedge\boldsymbol{\omega}) \tag{59}$$

of Eq. (15), which arise in the region to the rear of the point labelled S in Fig. 17, where the flow over the train in the tunnel separates, causing turbulence to progressively fill the region between S and the portal [39].

The length of the turbulent zone increases uniformly at the speed U of the train. The dominant contribution to p_D is the skin friction dipole (second member of Eq. (59)) — the contribution from interior vortex sources is of quadrupole strength and may be neglected; there is also a small additional contribution from the 'exit flow vortex' of Fig. 17, but this is usually small. The overall contribution from the turbulence sources can be

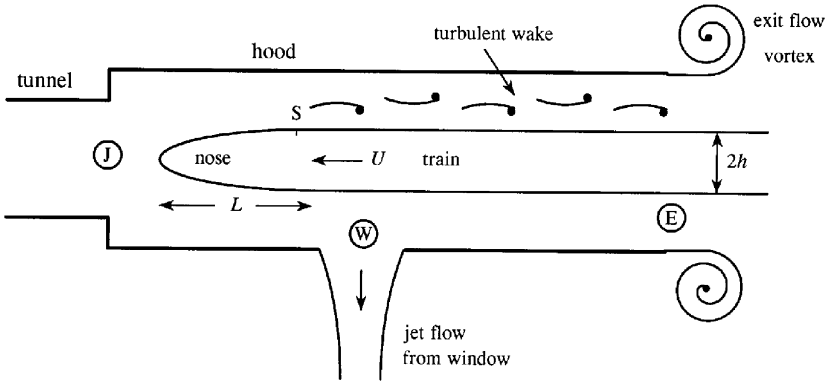

Fig. 17. Principal sources contributing to compression wave formation.

represented by (Howe and Iida [39])

$$p_D(\mathbf{x},t) = -\rho_o \int_{-\infty}^{\infty} \mathrm{d}\tau \oint_{S'} v_*^2(\mathbf{y},\tau)\, \frac{\partial G}{\partial y_1}(\mathbf{x},\mathbf{y},t,\tau)\, \mathrm{d}S(\mathbf{y}), \quad \mathbf{y} = (y_1,y_2,y_3), \tag{60}$$

where the surface integral is over those surface sections S' of the train and interior hood and tunnel walls 'wetted' by the separated flow, and $v_*(\mathbf{y},\tau)$ is the friction velocity on S'. If the front of the train nose is assumed to cross the entrance plane of the hood at $t = 0$, the integrand in Eq. (60) is null for $\tau < L/U$.

The characteristic length scale of $p_D \sim$ 'wetted length of the train'$/M$, and may therefore be calculated using the compact Green's function (51) by taking, for sources within the tunnel,

$$\frac{\partial G}{\partial y_1}(\mathbf{x},\mathbf{y},t,\tau) \approx -\frac{1}{2\mathscr{A}}\left\{\delta\left(t-\tau-\frac{(x-y_1)}{c_o}\right)+\delta\left(t-\tau+\frac{(x+y_1-2\ell_E)}{c_o}\right)\right\}. \tag{61}$$

The collective action of all surface elements of the train and tunnel subject to the turbulence fluctuations produces a predominantly steady drag force per unit surface area [39]. For the purpose of evaluating Eq. (60) it is therefore permissible to put $v_* = \mu U_{\mathrm{rel}}$ where μ is a constant 'friction factor' and U_{rel} is the mean turbulent flow velocity relative to the surface S' (which assumes different values on the surfaces of the train and tunnel walls).

Predictions of p_D from Eq. (60) for given train speed U depend on the value of the friction coefficient μ. The values of μ appropriate for model scale tests and at full scale are unlikely to be equal because of the overall absence of Reynolds number similarity, and because of the very significant differences in the effective surface roughness at model and full scale. For application to the case in Fig. 16 it is assumed that $\mu = 0.053$, which is seen to yield excellent agreement with the measured pressure.

5.4. *The flared portal*

A perfectly linear pressure rise across the compression wave front can be achieved by suitably *flaring* the tunnel portal over an axial distance ℓ, say, in the manner indicated in Fig. 18a. In this case the wavefront thickness $\sim \ell/M \gg \ell$ and the compact approximation should still be applicable. The acoustic problem is dynamically equivalent to calculating the pressure wave generated by the train together with its *image* in the rigid ground plane ($y = 0$) within a flared duct consisting of the tunnel and its image in the ground (Fig. 18b), which closely resembles the experiment in the photograph of Fig. 19 involving a flared duct of circular cross-section.

To find the function $\varphi_E^*(\mathbf{x})$ for use in Eq. (53) we assume that the tunnel cross-sectional area $S(x)$ decreases smoothly from $\mathscr{A}_E \equiv \pi R_E^2$ at $x = 0$ to the uniform value $\mathscr{A} = \pi R^2$ for $x \leqslant -\ell$. Changes in $S(x)$ are assumed to be sufficiently slow that φ_E^* satisfies the following simplified form of Laplace's equation within the tunnel [36]

$$\frac{1}{S(x)}\frac{\partial}{\partial x}\left(S(x)\frac{\partial \varphi_E^*}{\partial x}\right) = 0, \quad x < 0 \tag{62}$$

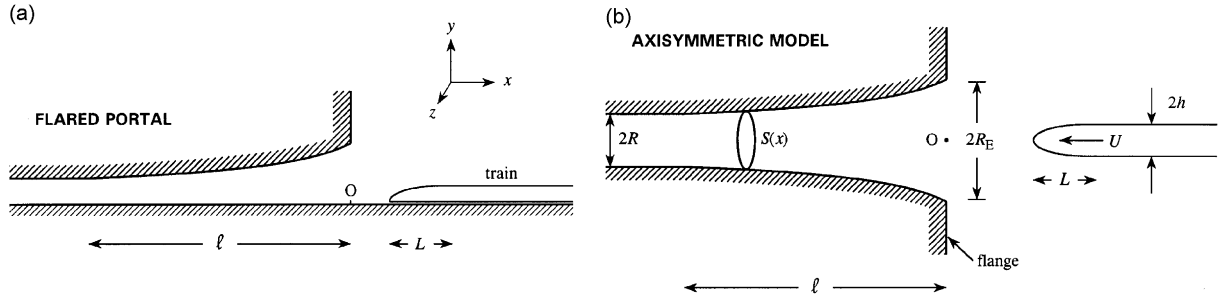

Fig. 18. (a) Train entering a tunnel with a flared portal of length ℓ; (b) axisymmetric flared portal.

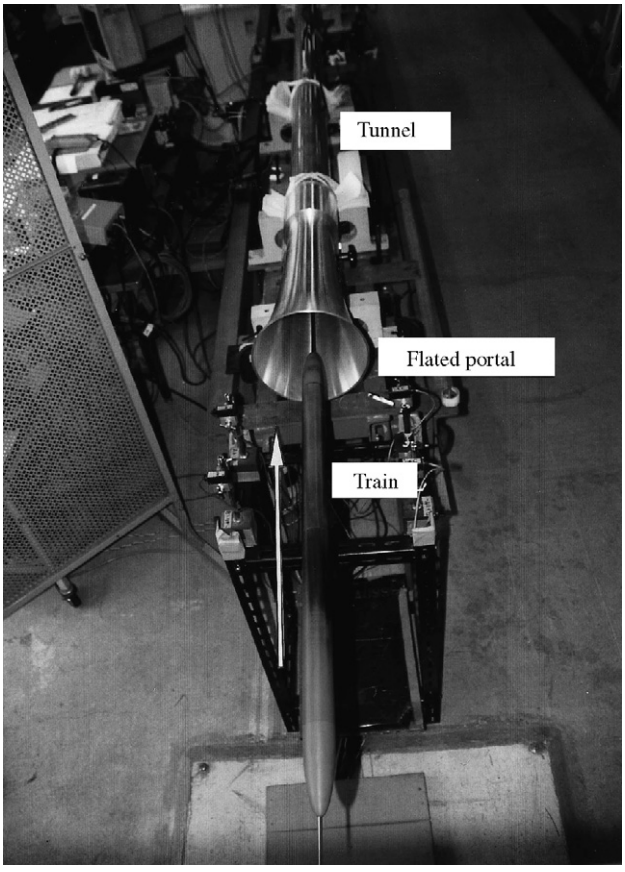

Fig. 19. Flared portal and cylindrical tunnel with a wire-guided axisymmetric model train [36].

with solution

$$\varphi_E^*(\mathbf{x}) = \mathscr{A}\int_0^x \frac{\mathrm{d}\xi}{S(\xi)} + C, \quad x<0, \tag{63}$$

where C is a constant. If the flange is taken to be infinite, the behaviour of $\varphi_E^*(\mathbf{x})$ outside the tunnel ($x>0$) is approximately the same as the potential of flow produced by a 'piston' of area $\mathscr{A}_E$ in a plane wall at $x=0$, moving with normal velocity $(\partial\varphi_E^*/\partial x)_{x=0} = \mathscr{A}/\mathscr{A}_E$. When $\mathbf{x}$ lies on the axis of symmetry (the x-axis), the

condition that $\varphi_E^*(\mathbf{x}) \to 0$ as $x \to +\infty$ then yields

$$\varphi_E^*(\mathbf{x}) = -\frac{\mathscr{A}R}{\mathscr{A}_E}\left[\left(\frac{\mathscr{A}_E}{\mathscr{A}}+\frac{x^2}{R^2}\right)^{1/2}-\frac{x}{R}\right], \quad x>0. \tag{64}$$

Equating expressions (63) and (64) at $x=0$, we find $C=-R\sqrt{\mathscr{A}/\mathscr{A}_E}$, and the end-correction is then given by

$$\ell_E = R\sqrt{\frac{\mathscr{A}}{\mathscr{A}_E}}+\int_{-\infty}^{0}\left(\frac{\mathscr{A}}{S(\xi)}-1\right)\mathrm{d}\xi. \tag{65}$$

To determine the functional form of the portal cross-section $S(x)$, consider again a 'snub-nosed' train for which $\mathscr{A}_T(s)/\mathscr{A}_o = H(s)$. Then Eq. (55) becomes

$$p_E \approx \frac{\rho_o U^2}{(1-M^2)}\left(1+\frac{\mathscr{A}_o}{\mathscr{A}}\right)\frac{\mathscr{A}_o}{S(-U[t])}, \quad U[t]/R>0, \tag{66}$$

after the nose has crossed the entrance plane into the flared section of the tunnel, where most of the pressure rise occurs. During this time $S(-U[t])$ decreases from $\mathscr{A}_E$ to $\mathscr{A}$, and the pressure rises from

$$\frac{\rho_o U^2}{(1-M^2)}\left(1+\frac{\mathscr{A}_o}{\mathscr{A}}\right)\frac{\mathscr{A}_o}{\mathscr{A}_E} \quad \text{to} \quad \frac{\rho_o U^2}{(1-M^2)}\left(1+\frac{\mathscr{A}_o}{\mathscr{A}}\right)\frac{\mathscr{A}_o}{\mathscr{A}}$$

at the respective instants at which the nose enters the tunnel portal and when the nose passes into the uniform section of the tunnel. This increase will have an optimal linear variation provided $1/S(-U[t])$ increases linearly with the retarded time, that is when

$$\frac{S(x)}{\mathscr{A}} = 1\Big/\left[\frac{\mathscr{A}}{\mathscr{A}_E}-\frac{x}{\ell}\left(1-\frac{\mathscr{A}}{\mathscr{A}_E}\right)\right], \quad -\ell<x<0. \tag{67}$$

If the length ℓ of the flared section is prescribed (i.e. when it is desired to have a compression wavefront of thickness $\sim\ell/M$), the value of the portal cross-section $\mathscr{A}_E$ is determined by requiring the pressure to vary smoothly at $U[t]/R=0$, when the nose enters the tunnel. This implies that $\partial^2\varphi_E^*(x,0,0)/\partial x^2$ defined by approximations (63) and (64) should be continuous at $x=0$, i.e. that

$$\frac{\mathscr{A}_E}{\mathscr{A}} = \left(\frac{\ell}{2R}\right)^{2/3}\left[\left(1+\sqrt{1-\left(\frac{2R}{3\sqrt{3}\ell}\right)^2}\right)^{1/3}+\left(1-\sqrt{1-\left(\frac{2R}{3\sqrt{3}\ell}\right)^2}\right)^{1/3}\right]^2. \tag{68}$$

The optimally flared portal should produce a smooth, linear compression wavefront when the snub-nosed train is replaced by one of the more realistic profile, provided the line source (50) defining the equivalent source strength of a smoothly profiled nose can be approximated by a suitably positioned *point source*. The photograph of Fig. 19 shows the model scale experiment performed at RTRI to test this hypothesis [36], involving a flared portal (shown with the *flange* removed) constructed to the above specifications when $R=50\,\mathrm{mm}$ and $\ell=500\,\mathrm{mm}$, so that $\mathscr{A}_E/\mathscr{A}=5.35$ and $R_E/R=2.31$ when $\ell/R=10$.

Fig. 20 illustrates a comparison of theory (Eq. (53)) and experiment ($\triangle\ \triangle\ \triangle$) when the optimally flared portal is *flanged*. The train nose is defined as in Eqs. (57) and (58) with $h=22.35$, $L=111.8\,\mathrm{mm}$, and for $R=50\,\mathrm{mm}$, $\ell=500\,\mathrm{mm}$, and the train speed $U=296\,\mathrm{km/h}$. The train is projected along the axis of symmetry and the nose enters the flared section at $U[t]/R=0$, following which the pressure rises linearly until just after its arrival at the uniform section of the tunnel at $U[t]/R\sim10$, producing a compression wave of thickness $\sim10R/M=207\,\mathrm{cm}$. Because of the large expansion in the cross-section of the tunnel at the portal, the contribution p_D from the turbulent drag is negligible, and is ignored.

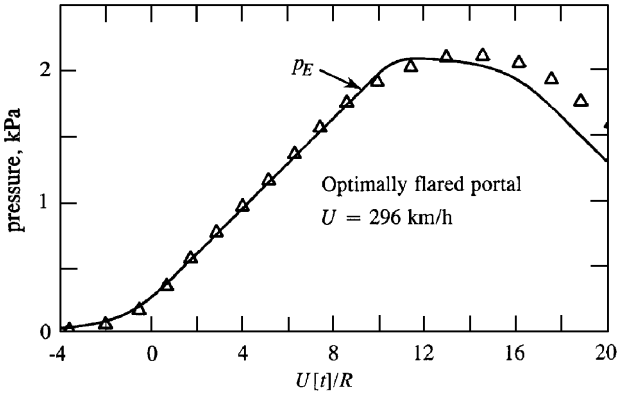

Fig. 20. Compression wave generated by a train with ellipsoidal nose entering at $U = 296\,\mathrm{km/h}$ a circular cylindrical tunnel of radius $R = 50\,\mathrm{mm}$ with an optimally flared portal of length $\ell = 500\,\mathrm{mm}$: △ △ △, pressure measured at a distance 1.55 m from the portal entrance plane; ——— Eq. (53).

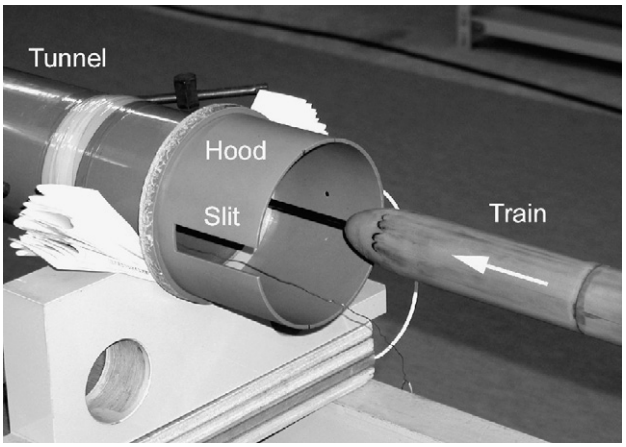

Fig. 21. Experimental 'short hood' with slit window showing an axisymmetric model train travelling along the 'far' track.

5.5. *Failure of the compact approximation*

The impending increase in operating speeds ($>350\,\mathrm{km/h}$) of high-speed rail networks has revealed a need to upgrade the current generation of tunnel entrance hoods. These are 'short hoods' typically of length ℓ_h equal to about twice the tunnel height. Fig. 21 illustrates a typical model scale circular cylindrical hood used to study compression wave generation in short hoods [40]. The model scale tunnel has internal radius $R = 50\,\mathrm{mm}$ and the circular cylindrical hood of internal radius $R_h = 1.25R$ has length $\ell_h = 2R$. According to Fig. 16b it might be expected that the compression wave thickness $\sim 2R/M \sim 6R$, and therefore that it is valid to treat the hood as acoustically compact for the purposes of calculating the compression wave. The compression wave pressure is then $p = p_E + p_D$, where in particular p_E is determined by the compact approximation (53) in terms of the potential function $\varphi_E^*(\mathbf{x})$, which must be determined by the numerical integration of Laplace's equation. This is easily done in the absence of windows, when the streamline pattern has the axisymmetric form shown in Fig. 22a. Along the path of the 'train' $\partial\varphi_E^*/\partial x$ decreases to zero outside the hood in two stages as x increases from negative values (Fig. 22b), and the compression wavefront would therefore be expected to exhibit a similar behaviour.

Predictions ($-\ -\ -$) of the compact approximation for $p(\mathbf{x}, t) = p_E(\mathbf{x}, t) + p_D(\mathbf{x}, t)$ and for the 'pressure gradient' $\partial p/\partial t$ are shown in Fig. 23 for a short, windowless hood ($R = 50\,\mathrm{mm}$, $R_h = 1.25R$, $\ell_h = 2R$) and for the ellipsoidal train nose defined by Eqs. (57) and (58) (with $h = 22.35\,\mathrm{mm}$, $L = 67.05\,\mathrm{mm}$) when the track

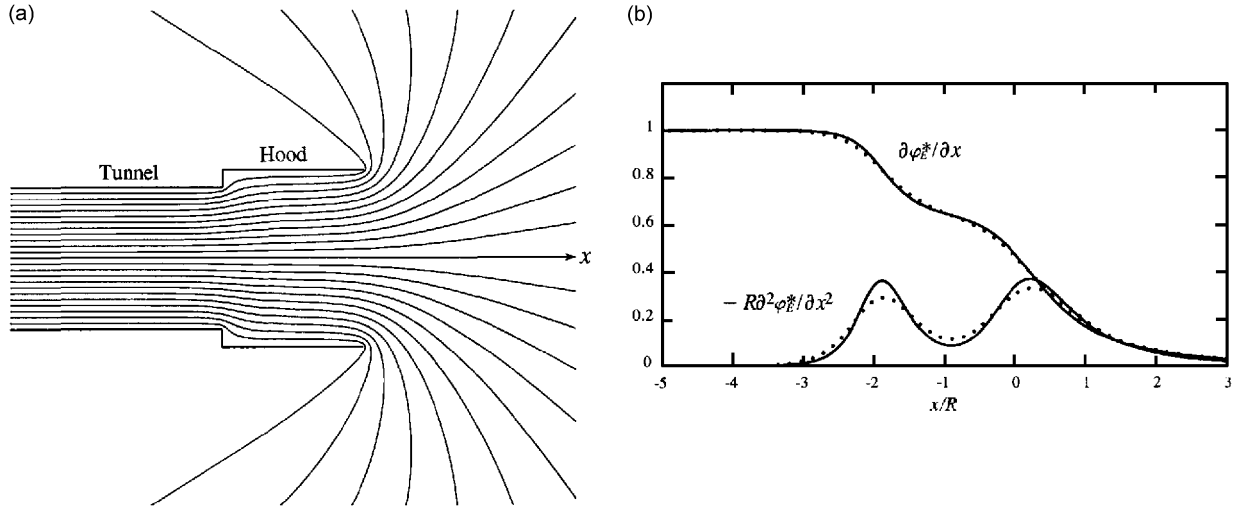

Fig. 22. (a) The streamline pattern of the potential flow from a short hood determined by $\varphi_E^*(\mathbf{x})$; (b) variations of $\partial\varphi_E^*/\partial x$ and $-R\partial^2\varphi_E^*/\partial x^2$ along $z_t = 0$ (• • •) and $z_t = 0.38R$ (——).

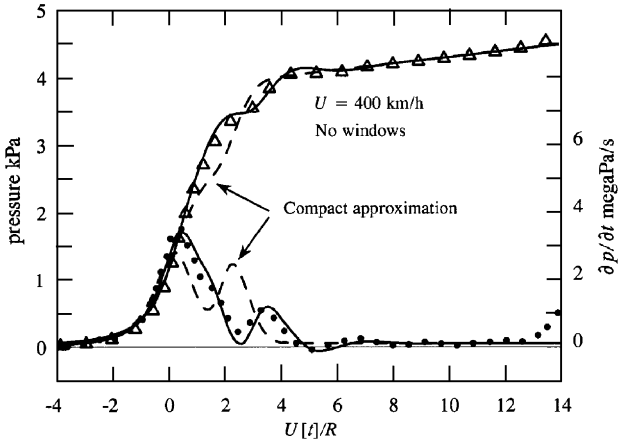

Fig. 23. Measured pressure (△ △ △) and pressure gradient (• • •) profiles compared with (i) the compact approximation (– – –) and (ii) the full prediction (——) for the hood of Fig. 22 and the ellipsoidal train nose defined by Eqs. (57) and (58) ($h = 22.35$ mm, $L = 67.05$ mm) when $z_t = 0.38R$, $U = 400$ km/h, $\rho_o = 1.182\,\mathrm{kg/m^3}$.

offset $z_t = 0.38R$, $U = 400\,\mathrm{km/h}$ ($M = 0.33$) and $\rho_o = 1.182\,\mathrm{kg/m^3}$. The predictions are qualitatively correct, but there are significant mismatches in phase and amplitude in the critical region of the compression-wave front, particularly noticeable when theory and experiment are compared for the subjectively important pressure gradient $\partial p/\partial t$. These differences indicate that important contributions to the overall phase of the wavefront are influenced by multiple reflections from the ends of the short hood, i.e. that the hood is *not* compact. The solid curves in Fig. 23 correspond to predictions of the 'noncompact' theory, the main points of which will now be summarized.

5.6. The noncompact hood without windows

The thickness of the compression wavefront exceeds the characteristic tunnel height R by a factor $\sim 1/M$, which is large even at the larger operating speeds involving Mach numbers ~ 0.4. Local interactions in a noncompact hood are therefore the same as for the compact case, but their relative *phases* must take account of the finite time of travel of sound waves between opposite ends of the hood.

The compression wave begins to form just before the train nose enters the hood (at the portal E in Fig. 17). The interaction of the train nose with the portal produces a compression wave that propagates as a plane wave ahead of the train and (in the absence of windows in the hood walls) subsequently interacts with the junction J of the hood and tunnel before the arrival of the train. At J the wave is partially transmitted into the tunnel and partially reflected back towards the entrance with (long wavelength values of the) transmission and reflection coefficients $\mathscr{R}_J$ and $\mathscr{T}_J$ given by

$$\mathscr{R}_J = \frac{\mathscr{A}_h - \mathscr{A}}{\mathscr{A}_h + \mathscr{A}} \quad \text{and} \quad \mathscr{T}_J = \frac{2\mathscr{A}_h}{\mathscr{A}_h + \mathscr{A}}. \tag{69}$$

The interaction of reflected waves with the train can be neglected in the usual case where $\mathscr{A}_o/\mathscr{A}_h \leqslant 0.2$. To a very good approximation, waves reflected back to the portal E can be assumed to be *totally* reflected at E with reflection coefficient $\mathscr{R}_E = -1$. In practice four or five back-and-forth reflections of p_E between opposite ends of the hood are necessary before most of the initial wave energy has passed into the tunnel.

The arrival of the train nose at junction J results in the generation of a second important pressure wave p_J, say, which propagates into the tunnel as a compression wave and back towards E as an expansion wave; again, the latter component of this wave experiences multiple reflections from the ends of the hood, but ultimately (after several round trips within the hood) most of its energy is transmitted into the tunnel and contributes to an extended profile of the compression wave front.

All of these interactions and multiple reflections are contained in the following noncompact extension of portal Green's function (51) [41]

$$G(\mathbf{x},\mathbf{y},t,\tau) = \frac{c_o\mathscr{T}_J}{2\mathscr{A}_h}\sum_{n=0}^{\infty}\mathscr{R}_E^n\mathscr{R}_J^n\left\{H\left([t]-\tau-\frac{(2n\ell+\varphi^*(\mathbf{y}))}{c_o}\right)\right.$$
$$\left.+\mathscr{R}_E H\left([t]-\tau-\frac{(2n\ell-\varphi^*(\mathbf{y}))}{c_o}\right)\right\},\ x\to-\infty \quad \text{(in the tunnel)}, \tag{70}$$

where $[t] = t + (x-\ell_E)/c_o$ is the retarded time and $\ell = \ell_h + \ell_E$.

The potential function $\varphi^*(\mathbf{x})$ represents the velocity potential of flow out of the portal E from $x=-\infty$, such that

$$\varphi^*(\mathbf{x}) \sim \begin{cases} x-\ell_E & \text{for } |x| \gg R_h \text{ within the hood,} \\ -\mathscr{A}_h/4\pi|\mathbf{x}| & \text{for } |\mathbf{x}| \gg R_h \text{ outside the hood,} \end{cases} \tag{71}$$

where the end-correction $\ell_E \approx 0.61R_h$ for a circular cylindrical portal [6].

To a good approximation $\varphi^*(\mathbf{x})$ can be approximated near E by the potential $\varphi_E^*(\mathbf{x})$ used in Eq. (51), for flow from a *semi-infinite* hood of radius R_h. In the neighbourhood of the junction J (at $x\sim-\ell_h$)

$$\varphi^*(\mathbf{x}) = \frac{\mathscr{A}_h}{\mathscr{A}}\varphi_J^*(\mathbf{x}) - (\ell_h+\ell_E), \tag{72}$$

where $\varphi_J^*(\mathbf{x})$ is the velocity potential of incompressible flow through the junction of two *semi-infinite* cylindrical ducts meeting at J, such that

$$\varphi_J^*(\mathbf{x}) \sim \begin{cases} x+\ell_h-\ell_j & \text{for } |x+\ell_h| \gg R \text{ in the tunnel,} \\ \dfrac{\mathscr{A}}{\mathscr{A}_h}(x+\ell_h) & \text{for } |x+\ell_h| \gg R_h \text{ in the hood,} \end{cases} \tag{73}$$

where $\ell_j \sim 0.05R$ is the effective 'length' of the junction [41]. The behaviour of $\varphi_J^*(\mathbf{x})$ near J can therefore be found using, say, a finite difference approximation to the equations for potential flow through a discontinuous change in cross-section in a circular duct infinite in both directions.

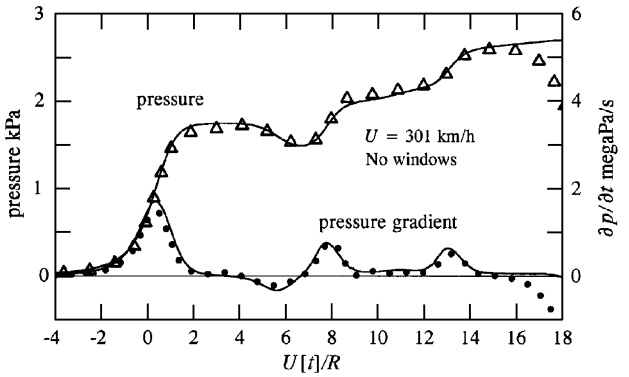

Fig. 24. Predictions of the compression wave pressure and pressure gradient (——) compared with experiment (△, •) for a model scale ellipsoidal nose train defined by Eqs. (57) and (58) ($h = 22.35$ mm, $L = 67.05$ mm) entering at $U = 301$ km/h a circular cylindrical tunnel with an unvented hood when $R = 50$ mm, $R_h = 1.25R$, $\ell_h = 10R$, $z_t = 0.4R$.

In terms of this modified Green's function, the net pressure wave p_H generated ahead of the train in the tunnel by the interaction of the train nose with both ends of the hood is found to be

$$p_H(\mathbf{x},t) \approx \frac{\rho_o U^2}{\mathscr{A}_h(1-M^2)}\left(1+\frac{\mathscr{A}_o}{\mathscr{A}}\right)\mathscr{T}_J\sum_{n=0}^{\infty}(-1)^n\mathscr{R}_J^n\int_{-\infty}^{\infty}\frac{\partial\mathscr{A}_T}{\partial x'}(x'+U[t]-2nM\ell)\frac{\partial\varphi_E^*}{\partial x'}(x',0,z_t)\,\mathrm{d}x'$$
$$+\frac{\rho_o U^2}{2\mathscr{A}(1-M^2)}\left(1+\frac{\mathscr{A}_o}{\mathscr{A}}\right)\mathscr{T}_J\sum_{n=0}^{\infty}(-1)^n\mathscr{R}_J^n\int_{-\infty}^{\infty}\left\{\frac{\partial\mathscr{A}_T}{\partial x'}(x'+U[t]-(2n-1)M\ell)\right.$$
$$\left.+\frac{\partial\mathscr{A}_T}{\partial x'}(x'+U[t]-(2n+1)M\ell)\right\}\frac{\partial\varphi_J^*}{\partial x'}(x',0,z_t)\,\mathrm{d}x'. \tag{74}$$

The first sum in this equation represents all components of the pressure produced by the interaction of the train nose with the portal E; the second consists of all those waves generated at time $\sim\ell_h/U$ later, as the train passes into the tunnel from the hood.

This formula replaces the much simpler expression (53) that is applicable in the absence of the hood. The net pressure radiated into the tunnel is now $p = p_H + p_D$, when the component p_D due to frictional forces is included. This combination has been used to plot the solid curves in Fig. 23 for the short hood.

Fig. 24 shows a comparison of theory and experiment for a *long* hood with $\ell_h = 10R$, when $U = 301$ km/h, $z_t = 0.4R$, ($M\sim0.25$) and $\rho_o = 1.23\,\mathrm{kg/m^3}$, $\mu = 0.053$. All other dimensions of the hood and train nose are the same as for the short hood of Fig. 23. The agreement between measurement and theory is maintained up to about $U[t]/R = 14$, after which the measured pressure falls off because of the imminent arrival of the train tail at the hood portal. Multiple reflections within the hood are responsible for the 'rippled' pressure profile and the 'pulsatile' pressure gradients shown in the figure. In contrast to the smooth and uniform pressure rise produced by the flared hood (Fig. 20), the effect of reflections is to cause a step-wise transmission of acoustic energy into the tunnel from the hood, so that although the compression wavefront is thickened by the hood (and, in particular, the maximum value of the subjectively important pressure gradient $\partial p/\partial t$ is reduced) the pressure rise is not uniform.

5.7. *Influence of hood windows*

A window may be regarded as a monopole acoustic source in the hood excited by the train. Consider the simplest case of a hood with *one* window (W in Fig. 17). When the wave generated as the train nose enters the hood portal E arrives at the window, the pressure at the wave front falls rapidly because the window initially behaves as a pressure node that generates an expansion wave p_W propagating in both directions away from the window. Vorticity production at the window quickly leads to the formation of a high-speed jet whose velocity

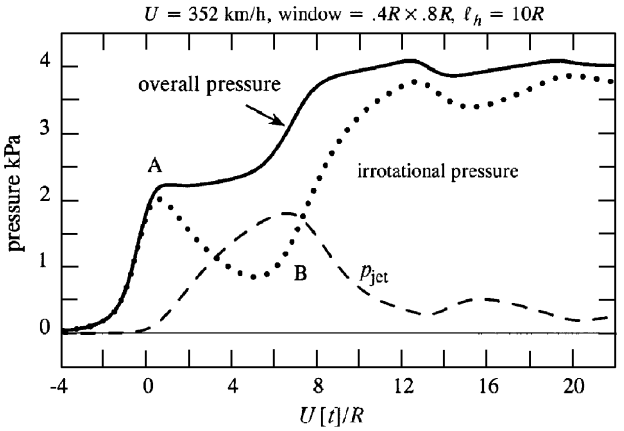

Fig. 25. Compression wave pressure for the model scale train defined by Eqs. (57) and (58) ($h = 22.35$ mm, $L = 67.05$ mm) when $U = 352$ km/h; $R = R_h = 50$ mm, and the hood wall has thickness $\ell_w = 0.1R$; there is one rectangular window of axial and azimuthal lengths $\ell_x = 0.8R$, $\ell_\theta = 0.4R$, centred at $x = -\ell_h = -10R$: (——) overall predicted pressure wave transmitted into the tunnel; (• • •) transmitted wave for irrotational window flow; (– – –) pressure pulse $p_{\rm jet}$ produced by the jet flow from the window.

increases typically to about 50% of the train speed. The jet vorticity is an aeroacoustic source, producing a pressure pulse that arrests the fall in pressure at the window, and causes the compression wave generated at the hood entrance to be transmitted past the window at reduced but constant amplitude. Subsequent reflections of this wave from the ends of the hood, and the additional pressure variations at W produced by the wave generated as the nose passes the junction J, also cause small fluctuations in jet velocity, but the most significant change in jet speed occurs when the train nose passes the window, following which pressure at the window decreases rapidly to a level only marginally higher than atmospheric and the radiation from the window into the tunnel decreases. In the meantime, once the nose has passed the window the pressure in front of the nose rises to a level comparable to the value it would have had if the window had been absent, causing the pressure at the rear of the compression wave front to rise. A similar but obviously more complicated set of interactions occurs in the presence of several windows, when in addition waves are reflected at the windows and the separate window jets are coupled by pressures reflected back and forth within the hood; these in turn produce further modifications of the compression wave front.

These remarks are illustrated in Fig. 25 for the simplest case of a single rectangular window positioned as in Fig. 15 with its centre at $x = -\ell_h = -10R$, when $R_h \equiv R$. The figure compares the predicted overall compression wave profile (——, for conditions given in the figure caption) with that (• • •) when the window flow is assumed to be irrotational (no jet). The irrotational pressure falls rapidly behind the wave front 'A'; the subsequent rise after 'B' is produced by the combined contributions of (i) the arrival of a second compression pulse from the hood portal after reflection of the expansion wave formed when the original wave front arrives at the window, and (ii) a reduction in the influence of the window caused by the decrease in volume flux occurring as the train nose passes the window. In the real flow, vorticity production at the window generates an additional pressure pulse $p_{\rm jet}$ (– – –) whose effect is to maintain the pressure just to the rear of the wave front 'A' at a roughly constant value until the initiation of mechanisms (i) and (ii) at 'B'. The pressure fields of the irrotational and rotational interactions combine to produce the overall compression wave profile. The window-generated pressure $p_{\rm jet}$ rises to a maximum at the retarded arrival time $U[t]/R \sim \ell_h/R - M(\ell_h + \ell_E)/R$ (≈ 7) of the train nose at the window, following which it decreases as the pressure forcing air out through the window becomes small.

To understand the nature of the radiation in the tunnel from the windows, note first that the pressure fluctuations produced at the window by the compression wave generated at the portal E or by a passing train have a time scale $\sim 2R_h/U$. In particular the corresponding

$$\text{compression wave front thickness} \sim 2R_h/M \approx 6R_h,$$

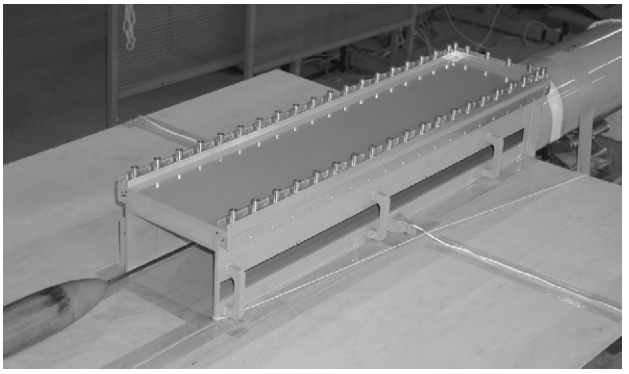

Fig. 26. Experiment involving a hood of rectangular cross-section with a long slit-window, including the effect of the ground plane [45].

which is typically much larger than a window diameter, so that the local tunnel pressure may be assumed to be uniform over the inner face of the window. This also turns out to be a good approximation for the dominant pressure fluctuation produced by the passage of the train nose past the window, determined analytically by considering the passage of the equivalent source distribution (50) past the window [42]. The air flow through the windows can then be calculated using empirical equations validated by Cummings for circular apertures [6,25,42–44] — the details are too involved to be discussed here but are described in full in Refs. [20,42].

Let $V_k(t)$ denote the mean jet velocity directed *out* of the hood in the plane of the kth window of area $\mathscr{A}_k$ whose centre is at $x = x_k$. Because the characteristic acoustic wavelength $\gg R_h$, the volume flow from the window generates two equal plane acoustic waves propagating in both directions away from the window within the hood. Before these waves interact with the ends of the hood or with any other window they produce a pressure fluctuation within the hood equal to

$$-\frac{\rho_o c_o \mathscr{A}_k}{2\mathscr{A}_h}\, V_k\left(t-\frac{|x-x_k|}{c_o}\right). \tag{75}$$

When V_k has been evaluated using the Cummings equations, the net pressure radiated into the tunnel from the kth window can be determined by taking account of multiple reflections of the pressure (75) from the ends of the hood, giving

$$\begin{aligned} p_k(\mathbf{x},t) = -\frac{\rho_o c_o \mathscr{A}_k}{2\mathscr{A}_h}\mathscr{T}_J \sum_{n=0}^{\infty}(-\mathscr{R}_J)^n\Bigg\{ V_k\left(t+\frac{\{x-x_k-2n(\ell_h+\ell_E)\}}{c_o}\right) \\ - V_k\left(t+\frac{\{x+x_k-2n(\ell_h+\ell_E)-2\ell_E\}}{c_o}\right)\Bigg\}, \quad x<-\ell_h. \end{aligned} \tag{76}$$

The overall compression wave within the tunnel now consists of the component p_H produced when the windows are ignored, $p_D(\mathbf{x},t)$ from the frictional drag and the contribution from each window:

$$p(\mathbf{x},t) = p_H(\mathbf{x},t) + p_D(\mathbf{x},t) + \sum_k p_k(\mathbf{x},t). \tag{77}$$

This formula has been used to calculate the results shown in Fig. 25.

As a final illustration (77) is applied to the experimental hood shown in Fig. 26 [45], which has a rectangular cross-section with the inner horizontal width equal to $2R = 150$ mm, the same as the maximum width of the tunnel, and length $\ell_h = 10R = 750$ mm. In this case the tunnel has a more realistic 'horseshoe' cross-section (not visible in the photograph, but such that the train blockage is still equal to 0.2.) and the hood height is 118.4 mm. The window extends along the whole of one side-wall in the form of a 735-mm-long horizontal slit of width 27 mm.

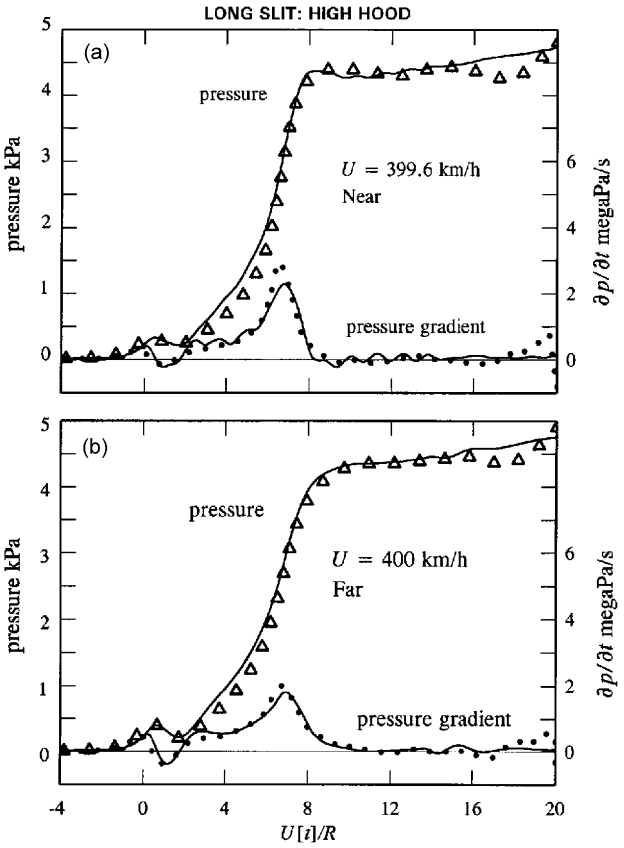

Fig. 27. Measured pressure (△ △ △) and pressure gradient (• • •) profiles and corresponding predictions (——) for an ellipsoidal train nose defined by Eqs. (57) and (58) ($h = 27.5$ mm, $L = 116$ mm) for the hood of Fig. 26 with a long slit window when $|z_t| = 0.44R$, $y_t = 0.5R$, $\mu = 0.047$: (a) $U = 399.6$ km/h, $\rho_o = 1.155$ kg/m^3, near; (b) $U = 400$ km/h, $\rho_o = 1.157$ kg/m^3, far.

The theory outlined above is strictly applicable for windows whose individual areas are small compared to the hood cross-section. The calculations for the slit are therefore performed by representing it by 10 adjacent windows of equal areas $A_k = 73.5 \times 27\,\text{mm}^2$, distributed uniformly along the hood wall at height $y_t = 0.5R$ above the ground plane (more details are given in Ref. [45]).

Theory and experiment are compared in Fig. 27a for a 'near' slit $z_t = 0.44R$ and in Fig. 27b for a 'far' slit with $z_t = -0.44R$. There is good overall agreement between the predicted and measured waveforms. Evidently the dominant effect of a long slit of relatively large open area is principally to delay the main pressure rise at the wavefront compared to the corresponding case of no windows. The main delayed pressure rise is practically equal to the full overall pressure rise (56) across the wavefront in the absence of the hood. A very 'open' slit extending the whole length of the hood therefore appears to vitiate the beneficial effects of reflections within the hood.

6. Conclusion

Lighthill was a strong advocate of the use of vortex methods in fluid mechanics. It was Powell [2], however, who pioneered the interpretation of vorticity as a source of sound. It is now recognized that a knowledge of the vorticity distribution in a complex flow–structure interaction is not only essential for a proper understanding of the mechanics of the motion, especially at low Mach numbers, but leads to the most effective means of calculating the acoustic noise produced by such flows.

The original acoustic analogy expresses the equivalence of sound production by a flow and the generation of sound in an ideal, stationary medium driven predominantly by Reynolds stress fluctuations. For homentropic

flow the theory can be recast into a form where vorticity alone may be identified as the ultimate acoustic 'source'. We have reviewed examples that show how the theory of sound production by vortex–surface interactions is greatly facilitated by the introduction of the 'compact' approximation to the acoustic Green's function in situations where the solid surface is acoustically compact or, more generally (for noncompact structures), where the surface supports locally compact regions of 'noisy' flow identified by the presence of singularities in the 'Kirchhoff vector'. These examples involve both rigid and deformable, compact and noncompact bodies of practical and pressing importance, and demonstrate how predictions of sound production in terms of vorticity frequently succumb to accurate analytical treatment when more conventional and general approaches by way of detailed numerical modelling of a source flow are intractable.

In principle, a noisy compressible flow can always be simulated numerically and an attempt made to predict the sound. There are, however, many flows that are just too complicated to be treated in this way in a timely manner — computation of the sound will then be possible only when it is known more definitely which factors have to be taken into account and which may be neglected. But when the dominant and noisy features of a flow have been recognised in this way it is often possible and more useful practically (as with the example of the compression wave generated by a high-speed train) to bypass a numerical treatment by judicious analytical modelling of the identified sources.

References

[1] M.J. Lighthill, On sound generated aerodynamically, part I: General theory, *Proceedings of the Royal Society of London Series A* 211 (1952) 564–587.

[2] A. Powell, Theory of vortex sound, *Journal of the Acoustical Society of America* 36 (1964) 177–195.

[3] J.E. Ffowcs Williams, The noise from turbulence convected at high speed, *Philosophical Transactions of the Royal Society of London Series A* 255 (1963) 469–503.

[4] J.E. Ffowcs Williams, D.L. Hawkings, Sound generation by turbulence and surfaces in arbitrary motion, *Philosophical Transactions of the Royal Society Series A* 264 (1969) 321–342.

[5] J.E. Ffowcs Williams, Sound production at the edge of a steady flow, *Journal of Fluid Mechanics* 66 (1974) 791–816.

[6] M.S. Howe, *Acoustics of Fluid–Structure Interactions*, Cambridge University Press, Cambridge, 1998.

[7] M.S. Howe, *Theory of Vortex Sound*, Cambridge University Press, Cambridge, 2003.

[8] S.C. Crow, Aerodynamic sound emission as a singular perturbation problem, *Studies in Applied Mathematics* 49 (1970) 21–44.

[9] D.G. Crighton, Basic principles of aerodynamic noise generation, *Progress in Aerospace Sciences* 16 (1975) 31–96.

[10] J.E. Ffowcs Williams, Aeroacoustics, *Annual Review of Fluid Mechanics* 9 (1977) 447–468.

[11] J.O. Hinze, *Turbulence*, second ed., McGraw-Hill, New York, 1975.

[12] N. Curle, The influence of solid boundaries upon aerodynamic sound, *Proceedings of the Royal Society of London Series A* 231 (1955) 505–514.

[13] D.G. Crighton, F.G. Leppington, On the scattering of aerodynamic noise, *Journal of Fluid Mechanics* 46 (1971) 577–597.

[14] D.G. Crighton, Scattering and diffraction of sound by moving bodies, *Journal of Fluid Mechanics* 72 (1975) 209–227.

[15] W.K. Blake, *Mechanics of Flow-induced Sound and Vibration*, *Vol.* 2: *Complex Flow–Structure Interactions*, Academic Press, New York, 1986.

[16] L.L. Beranek, I.L. Vér (Eds.), *Noise and Vibration Control Engineering*, Wiley, New York, 1992.

[17] D.G. Crighton, A.P. Dowling, J.E. Ffowcs Williams, M. Heckl, F.G. Leppington, *Modern Methods in Analytical Acoustics* (*Lecture Notes*), Springer, London, 1992.

[18] K.S. Brentner, F. Farassat, Helicopter noise prediction: the current status and future direction, *Journal of Sound and Vibration* 170 (1994) 79–96.

[19] M.S. Howe. Flow–structure interaction noise at low mach numbers, *Proceedings of the NATO Research and Technology Organisation Symposium on Ageing Mechanisms and Control*: *Part A — Developments in Computational Aero- and Hydroacoustics*, Manchester UK, 8–11 October 2001 (ISBN 92-837-0024-4).

[20] M.S. Howe, M. Iida, T. Maeda, Y. Sakuma, Rapid calculation of the compression wave generated by a train entering a tunnel with a vented hood, *Journal of Sound and Vibration* 297 (2006) 267–292.

[21] W. Möhring, Modelling low Mach number noise, in: E.-A. Müller (Ed.), *Mechanics of Sound Generation in Flows*, Springer, Berlin, 1980, pp. 85–96.

[22] B.B. Baker, E.T. Copson, *The Mathematical Theory of Huygen's Principle*, second ed., Oxford University Press, Oxford, 1969.

[23] L.D. Landau, E.M. Lifshitz, *Fluid Mechanics*, 2nd ed., Pergamon, Oxford, 1987.

[24] M.S. Howe, Contributions to the theory of aerodynamic sound, with application to excess jet noise and the theory of the flute, *Journal of Fluid Mechanics* 71 (1975) 625–673.

[25] G.K. Batchelor, *An Introduction to Fluid Dynamics*, Cambridge University Press, Cambridge, 1967.

[26] D.G. Crighton, The Kutta condition in unsteady flow, *Annual Review of Fluid Mechanics* 17 (1985) 411–445.

[27] W.R. Sears, Some aspects of non-stationary airfoil theory and its practical applications, *Journal of the Aeronautical Sciences* 8 (1941) 104–108.
[28] G. Fant, *Acoustic Theory of Speech Production*, Mouton, The Hague, 1960.
[29] J.L. Flanagan, *Speech Analysis Synthesis and Perception*, second ed., Springer, New York, 1972.
[30] K.N. Stevens, *Acoustic Phonetics*, MIT Press, Cambridge, MA, 1998.
[31] W. Zhao, C. Zhang, S.H. Frankel, L. Mongeau, Computational aeroacoustics of phonation, part I: Computational methods and sound generation mechanisms, *Journal of the Acoustical Society of America* 112 (2002) 2134–2146.
[32] M.S. Howe, R.S. McGowan, Sound generated by aerodynamic sources near a deformable body, with application to voiced speech, *Journal of Fluid Mechanics* 592 (2007) 367–392.
[33] G. Birkhoff, E.H. Zarantonello, *Jets, Wakes and Cavities*, Academic Press, New York, 1957.
[34] M.I. Gurevich, *Theory of Jets in Ideal Fluids*, Academic Press, New York, 1965.
[35] S. Ozawa, T. Maeda, T. Matsumura, K. Uchida, H. Kajiyama, K. Tanemoto, Countermeasures to reduce micro-pressure waves radiating from exits of Shinkansen tunnels, in: *Aerodynamics and Ventilation of Vehicle Tunnels*, Elsevier, Amsterdam, 1991, pp. 253–266.
[36] M.S. Howe, M. Iida, T. Fukuda, T. Maeda, Theoretical and experimental investigation of the compression wave generated by a train entering a tunnel with a flared portal, *Journal of Fluid Mechanics* 425 (2000) 111–132.
[37] M.S. Howe, The compression wave produced by a high-speed train entering a tunnel, *Proceedings of the Royal Society of London Series A* 454 (1998) 1523–1534.
[38] M.S. Howe, M. Iida, T. Fukuda, T. Maeda, Aeroacoustics of a tunnel-entrance hood with a rectangular window, *Journal of Fluid Mechanics* 487 (2003) 211–243.
[39] M.S. Howe, M. Iida, Influence of separation on the compression wave generated by a train entering a tunnel, *International Journal of Aeroacoustics* 2 (2003) 13–33.
[40] M.S. Howe, A. Winslow, M. Iida, Rapid calculation of the compression wave generated by a train entering a tunnel with a vented hood, part 2: Short hoods, *Journal of Sound and Vibration* 311 (2008) 254–268.
[41] M.S. Howe, M. Iida, T. Fukuda, Influence of an unvented tunnel entrance hood on the compression wave generated by a high-speed train, *Journal of Fluids and Structures* 17 (2003) 833–853.
[42] M.S. Howe, On the role of separation in compression wave generation by a train entering a tunnel hood with a window, *IMA Journal of Applied Mathematics* 70 (2005) 400–418.
[43] A. Cummings, Acoustic nonlinearities and power losses at orifices, *American Institute of Aeronautics and Astronautics Journal* 22 (1984) 786–792.
[44] A. Cummings, Transient and multiple frequency sound transmission through perforated plates at high amplitude, *Journal of the Acoustical Society of America* 79 (1986) 942–951.
[45] M. Iida, M.S. Howe, Compression wave generated by a high-speed train entering a tunnel fitted with a hood with a long slit window, *Journal of Low Frequency Noise, Vibration and Active Control* 26 (2007) 227–248.